Late Cretaceous evolution of chemical weathering at the northeastern South American margin inferred from mineralogy and Hf-Nd isotopes.

Pauline Corentin, Emmanuelle Pucéat, Pierre Pellenard, Michel Guiraud, Justine Blondet, Germain Bayon, Thierry Adatte

Late Cretaceous evolution of chemical weathering at the northeastern South American margin inferred from mineralogy and Hf-Nd isotopes

Pauline Corentin[1], Emmanuelle Pucéat[1], Pierre Pellenard[1], Michel Guiraud[1], Justine Blondet[1] Germain Bayon[2], Thierry Adatte[3]

[1]Biogéosciences, UMR 6282 CNRS, Université Bourgogne Franche-Comté, 21000 Dijon, France

[2]Univ Brest, CNRS, Ifremer, Geo-Ocean, F-29280 Plouzané, France

[3]Institute of Earth Sciences, Géopolis, University of Lausanne, Lausanne, Switzerland

Abstract

The origin of the global temperature decrease that initiated the last greenhouse-icehouse transition about 90 million years ago still remains debated. Among the potential processes driving long-term climate evolution over million-year timescales, this study investigates the possible impact of the uplift-weathering connection on the late Cretaceous atmospheric CO_2 drawdown and associated cooling.

We analysed a marine sediment record from the Demerara margin, using Nd and Hf isotopes in clay-size detrital fractions ($\Delta\varepsilon_{Hf(t)clay}$) together with bulk and clay mineralogy and major element abundances to reconstruct the evolution of tectonic uplift and chemical weathering intensity in northeastern South America during the late Cretaceous. Our data indicate that silicate weathering intensified on the northeastern South American margin during the middle Campanian and the Maastrichtian, concomitant with an uplift phase of the Guiana craton. We propose that the tectonic pulse highlighted by apatite fission track data,

argon/argon dating and primary silicate mineral evolution, was accompanied by an accelerated chemical weathering, which presumably acted as a sink for atmospheric CO_2. By contrast, during the earlier late Turonian to early Campanian, period of relative tectonic quiescence, climate most likely acted as the main driver controlling the evolution of chemical weathering intensity. The main phase of enhanced weathering induced by the uplift of the northeastern South American margin occurred during the Campanian, thereby postdating the onset of global seawater temperature decrease (late Turonian). By inference, this regional event is unlikely to have triggered late Cretaceous cooling but it may have acted as an additional factor stabilizing colder climate conditions at that time.

1. Introduction

The late Cretaceous was a period marked by major tectonic and climatic changes. While a global decrease of seawater temperature from the Turonian to the Maastrichtian is recorded by Tex_{86} and foraminiferal $\delta^{18}O$ proxy data at all latitudes, its origin remains unclear (Friedrich *et al.*, 2012 ; O'Brien *et al.*, 2017). A pronounced decrease in atmospheric CO_2 levels (pCO_2) at that time (Wang *et al.*, 2014) indicates that the late Cretaceous climate cooling was closely related to the global long-term carbon cycle. The same period was also characterized by major tectonic events such as the uplift of the West African and eastern South American margins (Harmann *et al.*, 1998 ; Gallagher & Brown, 1999 ; Jaspen *et al.*, 2012 ; Engelmann de Oliveira *et al.*, 2016 ; Green *et al.*, 2017, 2018 ; Mourlot *et al*., 2018 ; Roddaz *et al.*, 2021), which could have impacted the carbon cycle through enhanced mechanical erosion and chemical weathering.

Indeed, among the processes driving the long-term carbon cycle, chemical weathering of silicate rocks on continents acts as a major sink of atmospheric CO_2 over million-year

timescales. Chemical weathering depends on climatic parameters such as temperature and precipitation (White & Blum, 1995), but also on mechanical erosion rates. Continuous exposure of fresh rock surfaces by mechanical erosion promotes chemical weathering (Raymo & Ruddiman, 1988 ; West *et al.*, 2005 ; Gabet & Mudd, 2009), up to a threshold where, at high denudation rates, detrital material is exported too rapidly to further sustain silicate weathering in soils (West *et al*., 2005 ; Gabet & Mudd, 2009). In active tectonic settings, such kinetically-limited weathering regimes typically lead to near-constant chemical weathering rates with increasing denudation rates (White & Blum, 1995 ; Gabet & Mudd, 2009 ; West, 2012). Therefore, the relationship between tectonic uplift and silicate weathering, and thus the net impact of this process on atmospheric carbon concentrations, is not straightforward and still needs to be explored. The major uplift phase of South Atlantic margins during the late Cretaceous major climate change could provide new insights to explore the interplay between climate and tectonic uplift.

In this study, we investigated a marine sediment record from Demerara Rise (ODP Site 1259) to explore the response of silicate weathering to the uplift of the northeastern margin of the South American continent, which occurred during the late Cretaceous from Guiana to Brazil (McConnell, 1968 ; Harman, 1998 ; Morais Neto *et al.*, 2009 ; Jaspen *et al.*, 2012 ; Green *et al.*, 2018). A multi-proxy approach based on Hf-Nd isotope analyses of clay-size detrital fractions combined with complementary geochemical and mineralogical data can provide unique insights into the evolution of continental chemical weathering through time (Bayon *et al.*, 2016 ; Corentin *et al.*, 2022; Bayon *et al*., 2022). Recently, the same approach has been successfully used to reconstruct the late Cretaceous evolution of silicate weathering along the southeastern Brazilian margin (Corentin *et al.*, 2022), showing that the formation of high topographic relief under arid climate conditions favoured mechanical erosion until the

elevation was high enough to support high orographic precipitations and, consequently, enhanced silicate chemical weathering (Corentin *et al.*, 2022).

2. Setting

ODP Site 1259 (2354 meter depth) from Demerara Rise (Fig. 1) exhibits upper Cretaceous sediments from the Cenomanian to the Maastrichtian (Erbacher *et al.*, 2004). The samples were collected from two lithostratigraphic units (between 440 and 540 mbsf; Fig. 2, 3) : 1) a Turonian to Santonian interval composed of laminated calcareous claystone with organic matter, clayey chalk and limestone; and 2) a Campanian to late Maastrichtian interval, composed of nannofossil-rich clayey chalk, calcareous siltstone and glauconitic claystone (Fig. 2, 3 ; Supplementary Table 1 ; Erbacher *et al.*, 2004). These sediments were deposited in a marine setting evolving from shelf environments during the Cenomanian to upper bathyal environments in the early Campanian (Erbacher *et al.*, 2005), under direct influence of terrigenous fluxes from the adjacent continental margin (März *et al.*, 2009).

The Demerara Rise, surrounded by the Guiana/Suriname (GS) and the Foz do Amazonas (FOZ) basins, is located on the northeastern South American margin (Fig. 1.A, 1.B), near the Guiana, Suriname and French Guiana coastal regions (Fig. 1.B). During the end of the early Cretaceous, a plate kinematic reorganization (~ 105 Ma), followed by a late Cenomanian-Turonian deformation led to the uplift of the Demerara plateau (Yang and Escalona, 2011; Basile *et al.,* 2013; Loncke *et al.,* 2020). The plateau became a structural high separating the Guiana/Suriname Basin and the Foz do Amazonas Basin and resulting in the isolation the Demerara plateau (Fig. 1.B; Loncke *et al.,* 2020). After the late Albian unconformity, the Demerara plateau evolved into a passive margin with a transition from shallow to deep marine conditions (Loncke *et al.,* 2020).

The Guiana Shield represents the main continental landmass that provides detrital sediment inputs to the Demerara Rise (Roddaz *et al.*, 2021 ; Fig. 1.B). During the late Cretaceous, this area corresponded to a low-elevation passive margin located in a humid equatorial climatic belt (Hay *et al.*, 2012 ; Sapin *et al.*, 2016).

3. Material and methods

A total of 88 samples from Site 1259 were analysed, spanning a period from the late Turonian to late Maastrichtian. The age model is based on the biostratigraphy published in Erbacher *et al.* (2004) and Gradstein *et al.* (2012).

3.1. Mineralogical analyses

Bulk sediment and clay (< 2 μm) mineralogical analyses were performed at the Biogeosciences Laboratory (University of Burgundy, France) using X-ray diffraction (XRD) with a Bruker Endeavor D4 diffractometer equipped with a Lynxeye detector, CuKα radiations and Ni filter, under 40 kV voltage and 25 mA intensity. The isolated clay fraction was analysed using the three treatments recommended by Moore and Reynolds (1997). Identification and semi-quantification of the mineral phases were performed with the software MacDiff 4.2.5 (Petschick, 2001) using the position of mean diffraction peaks and the area of their main diffraction peaks, respectively. For clay mineralogy, the proportions were estimated after ethylene glycol solvated preparation using the main diffraction (d_{001}) peak.

The (Illite+Chlorite)/smectite ((I+C)/S), (Opal+Clinoptilolite)/Calcite ((O+C)/Ca) and Feldspar/Clays (Feld./Clays) ratios were calculated using the mean peak area of each mineral. The uncertainty of the relative proportions of clay minerals is estimated as < 5%, based on replicate analyses of samples and the internal procedure of quantification using MacDiff on mixtures of clay minerals in known proportions.

121 The clay fractions of 3 samples were dispersed in distilled water and butylamine solution,
122 and deposited on a carbon formvar Cu grid for Transmission Electron Microscopy (TEM) ob-
123 servations. Images of clay particles were performed using a MET Hitachi 4800 at the INRAE
124 of the University of Burgundy (France).

125 3.2. Geochemical analyses

126 Major element abundances and CIA

127 X-ray fluorescence spectroscopy (XRF) was used to determine whole-rock major element
128 abundances (SiO_2, TiO_2, Al_2O_3, Fe_2O_3, MnO, MgO, CaO, Na_2O, K_2O and P_2O_5;
129 Supplementary Table 1) at the University of Lausanne, using a wavelength-dispersive
130 PANalytical AxiosmAX spectrometer fitted with a 4 kW Rh X-ray tube. Fused disks were
131 prepared from 1.2 g of calcined sample powder mixed with lithium tetraborate (1:5 mixture)
132 for the analyses. A number of 21 international silicate rock reference materials was used for
133 the calibration. The data are reported on a loss of ignition (LOI)-free basis (Supplementary
134 Table 1). The limits of detection are in the range 20 to 80 ppm for major elements depending
135 on the element concerned.

136 The chemical index of alteration (CIA) was calculated and used as a proxy of chemical
137 weathering intensity (Nesbitt & Young, 1982). Because our samples of bulk sediments
138 display relatively high carbonate contents (between 14-91 %), detrital CaO contents were
139 estimated using the method of McLennan (1993), which consists of replacing CaO* by Na_2O
140 in the following calculation: (Al_2O_3/[Al_2O_3 + Na_2O + CaO* + K_20] x 100 (where CaO*
141 represents the amount of CaO in the silicate fraction of the sediments). The CIA is generally
142 interpreted as the extent to which feldspar, which contains relatively mobile Ca, Na and K,
143 has been weathered and converted to Al-rich clay minerals (Nesbitt & Young, 1982).

144 Hf, Zr and REE concentrations and Hf-Nd isotopes

Following the protocol described in Bayon *et al.* (2002) and modified in Corentin *et al.* (2022), a total of 23 samples (8 samples collected in claystone lithology and 15 samples collected in chalk lithology ; Supplementary Table 1) were selected for geochemical analyses. This protocol includes a sequential leaching procedure that successively removes carbonates, Fe-Mn oxyhydroxides and organic matter. Then, the clay-size detrital fraction (< 2µm) is separated from the residual sediments by decantation and submitted to a second leaching procedure. Following clay extraction, about 65 mg of dry powdered samples were digested by alkaline fusion after addition of a Tm spike (Barrat *et al.*, 1996).

Finally, ion exchange chromatography was used to isolate purified Nd and Hf fractions using columns packed with AG-50W-X8 and Ln-Spec resin for Nd and AG1-X8 and Ln-Spec for Hf, following the protocols described in Chu *et al.* (2002) and Bayon *et al.* (2012), respectively.

Concentrations of REE, Hf and Zr were measured by inductively coupled plasma mass spectrometry (ICP-MS) on a Thermo Scientific X-Series II at the Pôle Spectrométrie Océan (Brest, France). Details about measured elemental masses, polyatomic interference corrections and the quantification method are given in Barrat *et al*. (1996) and Bayon *et al.* (2009b). External reproducibility and accuracy were estimated by replicate analyses of four certified reference materials from the United States Geological Survey (BCR-2, BIR-1, MAG-1, BHVO-2 ; Supplementary Table 2). Analytical reproducibility was better than 2% for all elements. Deviations from the reference values for BHVO-2, BCR-2 and BIR-1 (Jochum *et al.*, 2016) were always < 10% RSD.

Hafnium and neodymium isotope compositions of studied samples were measured on a MC-ICP-MS Neptune Plus (Thermo Scientific) at the ENS of Lyon (France) with a sample-standard bracketing method, using concentration-matched solutions of JMC475 and JNdi-1 standards, respectively. The instrumental mass bias were corrected applying an exponential

law, using $^{146}Nd/^{144}Nd = 0.7219$ and $^{179}Hf/^{177}Hf = 0.7325$. Nd and Hf procedural blanks were respectively better than 6 pg and 10 pg.

The analytical session gave a $^{176}Hf/^{177}Hf$ ratio of 0.282163 ± 0.000008 (2 s.d., n=21) corresponding to an external reproducibility of ± 0.28ε (2 s.d.) based on repeated analyses of JMC 475 standard solutions (at 35, 30 or 20 ppb). Replicate analyses of the BHVO-2 reference material gave a $^{176}Hf/^{177}Hf$ value of 0.283108 ± 0.000005 (2 s.d., n=3), in agreement with the reference values of 0.283096 ± 0.000020 (Weis *et al.*, 2005).

The analytical session gave a $^{143}Nd/^{144}Nd$ ratio of 0.512115 ± 0.000007 (2 s.d., n=14), corresponding to an external reproducibility of ± 0.14 ε (2 s.d.) based on repeated analyses of bracketed JNdi-1 standard solution (at 40 ppb). Repeated analyses of the BHVO-2 and BCR-2 reference materials gave respectively a $^{143}Nd/^{144}Nd$ value of 0.512984 ± 0.000006 (2 s.d., n = 3) and 0.512643 ± 0.000005 (2 s.d., n = 3), respectively, agreeing well with published values of 0.512990 ± 0.000010 and 0.512638 ± 0.000015 (Weis *et al.*, 2006).

The Hf isotope data are reported using the standard notation $\varepsilon_{Hf(t)} = [((^{176}Hf/^{177}Hf)_{sample}/(^{176}Hf/^{177}Hf)_{CHUR}) - 1] \times 10^4)$, corrected for the radioactive decay of ^{176}Lu to ^{177}Hf based on Hf and Lu concentrations measured for each sample ($^{176}Lu/^{177}Hf$ = Lu/Hf x 0.1424), the absolute age (t) calculated using the age model of Erbacher *et al.* (2004) and the timescale of Gradstein *et al.* (2012), and the ^{176}Lu radioactive decay constant λ (1.867×10^{-11} an^{-1} ; Söderlund *et al.*, 2004). The initial $^{176}Hf/^{177}Hf$ ratio of the CHondritic Uniform Reservoir was calculated using the present-day CHUR value of 0.282785 and a $^{176}Lu/^{177}Hf$ ratio of 0.0336 (Bouvier *et al.*, 2008).

The Nd isotope data are reported using the standard notation $\varepsilon_{Nd(t)} = [((^{143}Nd/^{144}Nd)_{sample}/(^{143}Nd/^{144}Nd)_{CHUR}) - 1] \times 10^4)$ corrected for the radioactive decay of ^{147}Sm to ^{143}Nd based on measured Nd and Sm concentrations ($^{147}Sm/^{144}Nd$ = Sm/Nd x 0.6049), the absolute age (t) and the ^{147}Sm radioactive decay constant λ (6.54×10^{-12} an^{-1} ;

195 Lugmair & Marti, 1977). The $^{143}Nd/^{144}Nd$ ratio of CHUR was calculated using the present-
196 day value of 0.512630 and a $^{147}Sm/^{144}Nd$ ratio of 0.1960 (Bouvier *et al.*, 2008).

197 *4. Results*

198 4.1. Bulk and clay mineralogy

199 The bulk sediment assemblage (Fig. 2 ; Supplementary Table 1) is composed of clays (0 to
200 36%), quartz (0.5 to 28%), K-feldspar (0 to 5%), calcite (14 to 98 %), plagioclase (0 to 11%),
201 opal-CT (0 to 58 %), clinoptilolite (0.6 to 19 %), pyrite (0 to 5 %), gypsum (0 to 10 %) and
202 traces of dolomite (≤ 1 %). From the Turonian to Santonian, a rich assemblage is composed of
203 all the identified minerals. After the Santonian, the proportions of clinoptilolite, pyrite,
204 gypsum and dolomite decrease and these minerals progressively disappeared (Fig. 2). The
205 main mineralogical evolution concerns variations in the carbonate and siliceous mineral
206 content. A net increase of the opal-CT and low-quartz content is indeed observed in the
207 Santonian to Campanian interval balanced by an apparent decrease of calcite following an
208 episode marked by an increase in clinoptilolite (Fig. 2). The plagioclase and K-feldspar
209 proportions also present a slight increase from the Coniacian to the Campanian, then record a
210 decrease from the Campanian to the Maastrichtian as well as the quartz content while the
211 proportions of clay slightly increased (Fig. 2).

212 Clay mineralogy data show that clay-size fractions at Site 1259 are dominated by smectite
213 (~85 to 100 %), with minor amounts of illite and palygorskite (both up to ~8 %), and traces of
214 kaolinite and chlorite (Fig. 3 ; Supplementary Table 1). Note that chlorite contents are
215 negligible (<1 %). Clay mineral assemblages do not present major changes along the studied
216 interval. The Turonian samples present the highest proportions of illite and palygorskite, up to
217 8%, which then decrease and remain lower than 5% from the Coniacian to the Maastrichtian
218 apart from a slight increase in illite during the Coniacian-Campanian interval (Fig. 3).

219

220 4.2. Major elements

221 Major elements were measured in the bulk sediments and gave a wide range of concentrations
222 (Table 1). The elements content vary from 1.70 to 59.93 % (mean 21.90 %) for SiO_2, from
223 0.48 to 8.11 % (mean 3.83 %) for Al_2O_3 and from 0.02 to 0.33 % (mean 0.16 %) for TiO_2.
224 The K_2O content vary from 0.01 to 1.62 % (mean 0.44 %), the CaO content from 12.37 to
225 52.91 % (mean 31.71 %) and the Na_2O content from 0.03 to 1.63 % (mean 0.82 %). Finally,
226 the content vary from 0.03 to 1.59 % (mean 0.396 %) for P_2O_5, from 0.16 % to 4.30 % (mean
227 1.33 %) for Fe_2O_3, from 0.01 % to 0.08 % (mean 0.02 %) for MnO, from 0.47 % to 1.46 %
228 (mean 0.76 %) for MgO and from 0 % to 0.03 % (mean 0.01 %) for the Cr_2O_3.

229

230 4.3. Hf, Zr and REE concentrations

231 The rare earth and trace elements concentrations are reported in Table 1. The analysed clay
232 fraction displays zirconium (Zr) concentrations between 42 and 157 ppm that are in the range
233 of modern zircon-poor clay-size fraction (Bayon et al., 2016). Rare Earth Element
234 concentrations of the samples (Table 1) have been normalized to Post-Archean average
235 Australian Shale (PAAS; Taylor et McLennan, 1985), with REE patterns displayed on Fig. 4.
236 Most of the samples present a relatively flat pattern as expected for detrital clays (Fig. 4), that
237 is also highlighted by their position in the "flat" REE pattern domain in a crossplot (Fig.5B)
238 MREE/MREE* (MREE : Middle Rare Earth Elements) versus HREE/LREE (Heavy Rare
239 Earth Elements/Light Rare Earth Elements), except for three samples (at 494.26 m, 494.74 m
240 and 506.05 m) that display a slight enrichment in HREE and a slight negative cerium anomaly
241 (Ce/Ce*) between about 0.5 and 0.7). Figure 5.A presents a crossplot HREE vs Ce/Ce*
242 highlighting the position of these three samples compared to the remaining of the samples

243

244 4.4. Hf-Nd isotopes

245 The $^{143}Nd/^{144}Nd$ and $^{176}Hf/^{177}Hf$ ratios and the $\varepsilon_{Nd(t)}$ and $\varepsilon_{Hf(t)}$ values are provided in Table
246 2. The Nd isotope composition of studied samples displays unradiogenic values from -13.8 in
247 the Turonian to -15.7 in the Campanian, reaching -17.5 in the late Campanian following a
248 positive excursion with values up to -12.3 (Figs. 3, 6). A slight increase is observed during the
249 Maastrichtian with values up to -15.6. The Hf isotope composition of the studied samples
250 displays unradiogenic values between -12.2 to -6.0 (Fig. 3, 6). They first decrease from values
251 of about -7.4 during the Turonian to values of about -12.2 in the Coniacian, then increase
252 from the Campanian to the end of the Maastrichtian where they reach values of about -6.1.
253 Finally, calculated $\Delta\varepsilon_{Hf(t)clay}$ values at Demerara Rise decrease from the end of the Turonian to
254 the Santonian – earliest Campanian, from -1.3 to -5.1 (Fig. 3). Then, $\Delta\varepsilon_{Hf(t)clay}$ values increase
255 during the Campanian until the end of Maastrichtian with values up to - 0.1 (Fig. 3).

256

257 *5. Discussion*

258 5.1. Influence of authigenesis and diagenesis on mineralogical and geochemical signals

259 Clay mineral assemblages at Site 1259 are dominated by smectite, what is a common
260 feature of upper Cretaceous marine sediment sequences, which were shown to be mainly of
261 detrital origin (Robert, 1981 ; Chamley, 1989). This is further corroborated by TEM
262 observations (Fig. 7.B), which reveal the presence of flaky shape smectite particles, with no
263 evidence of lath-type overgrowths characteristic of clay authigenesis (Clauer *et al.*, 1990).
264 However, three samples at 494.26 m, 494.74 m and 506.05 m (80.25, 83.36 and 89.15 Ma) are
265 marked by a slight negative cerium anomaly, down to 0.53, and slight enrichments in heavy

rare earth elements, (Figs. 4, 5) which could possibly indicate the presence of a seawater signal associated with authigenic clay formation (Fagel, 1992 ; Figs. 4, 5).

Interestingly, these three samples presenting some evidence of clay authigenesis formation, althought limited, also yield more radiogenic (less negative) ε_{Nd} values (Fig. 3, 8 ; Table 2).

At Demerara Rise, $\varepsilon_{Nd(t)}$ seawater values inferred from fish tooth ε_{Nd} are quite negative during the late Cretaceous, around -16 on average over most of the interval although excursions toward more radiogenic values have been recorded during Oceanic Anoxic Event 2 (OAE2, Cenomanian-Turonian), up to -8, and at the end of the Maastrichtian (Fig. 8; MacLeod et al., 2008; Martin et al., 2012). Although the origin of the radiogenic excursion of seawater $\varepsilon_{Nd(t)}$ during OAE2 still remains discussed, it has been interpreted as reflecting the input of more radiogenic tethyan seawater at Demerara Rise. As Demerara Rise represented a bathymetric high (Loncke *et al*., 2020), it may have been potentially more affected by changes in oceanic currents than other parts of the margin basins. Unfortunately, no seawater ε_{Nd} data are available at Demerara Rise for the period encompassing the three clay samples that present a slight negative Ce anomaly, a slight HREE enrichment, and more radiogenic $\varepsilon_{Nd(t)}$ values. Thus, it is not possible to determine if this interval was associated with more radiogenic seawater $\varepsilon_{Nd(t)}$ values at Demerara Rise as it was observed for OAE2 and the late Maastrichtian, that could explain a deviation of clay ε_{Nd} toward more radiogenic values if authigenic clays formed at that time and integrated this more radiogenic seawater signal. Alternatively, post-depositional alteration of volcanogenic material linked with active volcanism from the CLIP (Caribbean Large Igneous Province) and/or the Bahamas hot spot (Roddaz *et al.*, 2021) would also result in authigenic smectite formation with a quite radiogenic Nd signature. Sporadic excursions of clay Nd isotope composition toward more radiogenic values have also been reported by Roddaz *et al.* (2021), interpreted as reflecting either an increase in the proportion of radiogenic material eroded from ancient mafic sources

exposed on the continent, or as the occurrence of volcanogenic inputs. Such input of mafic/volcanogenic material would be expected to induce an Eu anomaly in the REE spectra of the 3 samples with more radiogenic $\varepsilon_{Nd(t)}$ values, which is not observed here (Fig. 4; supplementary figure 3).

According to the literature, the sediment interval associated with the most radiogenic sample (Core 18 section 7 at 494.26 m ; Fig. 3) also contains a glauconitic level interpreted as an evidence of very low sedimentation rates (Friedrich & Erbacher, 2006 ; Nederbragt *et al.*, 2007 ; März *et al.*, 2009). This condensed interval is also characterized by the hiatus observed between the Coniacian and the Campanian, which marks the lithological transition between claystones and marly-chalks (Fig. 3). This particular event may have been induced by the Santonian-Campanian transgression that led to more open oceanic conditions (Haq, 2014). The observation of smear slides, performed on two samples from the bottom of the core, including the sample presenting the highest (most radiogenic) Nd values, clearly reveals the occurrence of glauconite (Fig. 7.A), hence confirming localized neoformed clay minerals. Low sedimentation rates and a decrease of detrital supply to the site would have favoured the formation of authigenic smectite and glauconite, potentially enhanced by in situ weathering of volcanogenic material deposited during this period.

The presence of glauconite observed in smear slide and previously described in the core (Erbacher *et al.*, 2004), could possibly lead to an overestimation of illite contents as these two clay minerals have overlapping diffraction peaks that cannot be distinguished by XRD analyses. However, smear slide observations show that only some samples of core 18 are marked by the presence of glauconite while the other levels displaying high illite contents (Fig. 3) do not contain glauconite, confirming that most of clays are detrital for the Demerara Rise site. Palygorskite in marine sediments can also be formed during marine authigenic

315 processes, but TEM observations indicate short and broken palygorskite fibres characteristic
316 of a detrital origin (Fig. 7.B).

317 Apart from the 3 samples with some evidence of clay authigenesis and partial
318 incorporation of a seawater signal, all other clay-size fractions present flat shale-normalized
319 rare earth element (REE) patterns and an absence of any Ce anomaly (Ce/Ce* above 0.7 ;
320 Roddaz *et al.*, 2021 ; Fig. 4, 5) and corresponds to the "Shale" fields in figure 5.B , thereby
321 indicating a detrital origin for the late Cretaceous clays at Demerara Rise, as already pointed
322 out by Roddaz *et al.* (2021). This is also coherent with the interpretation of März *et al.* (2009),
323 who showed, based on major and trace element composition, that detrital sediments deposited
324 at the Demerara Rise during the late Cretaceous were essentially derived from the erosion of
325 the adjacent Guiana-Suriname margin. Overall, clay minerals at Site 1259 appear mostly
326 inherited from nearby continental landmasses, with only limited and sporadic influence of
327 authigenesis (i.e. glauconite, volcanogenic smectite) along the studied sediment sequence.

328 In the bulk sediment, a net increase in quartz abundance also appears in the Santonian-
329 Campanian interval. However, this increase is also matched by higher opal-CT contents (up to
330 58% of the bulk sediment, Fig. 2). Quartz may also have a marine biogenic origin by
331 transformation of opal-CT during early diagenesis (associated to temperature lower than
332 60°C) in marine sequence around 400 meters burial depth (Hesse, 1988). Thus, its
333 concomitant evolution with opal-CT suggests that the increase of quartz is likely associated to
334 biogenic processes and may in this case correspond to microquartz associated to opal-CT both
335 deriving from opal-A (Riech & von Rad, 1979; Hesse, 1988). It has also been reported that
336 calcareous sediments favour the direct transformation of opal-A into quartz while
337 transformation of opal-CT into quartz is enhanced if detrital quartz is present (Hesse, 1988),
338 which may explain the net increase of quartz in the Santonien-Campanien. For this interval,
339 sediment is probably composed of mixed detrital and biogenic microquartz, impeding the use

of quartz content to track variations in detrital inputs. Zeolites (i.e. clinoptilolite, Fig. 2) and opal-CT are also formed authigenically by dissolution of amorphous SiO_2 most likely derived from dissolution-reprecipitation of siliceous organisms (März et al., 2009). We have therefore calculated the ratio (Opal+Clinoptilolite)/Calcite ((O+C)/Ca ; Fig. 8) in order to track the variability of marine primary productivity, as it was demonstrated that clinoptilolite was a good proxy of enhanced biogenic silica productivity (e.g. Karpoff et al., 2007).

5.2. Sources and detrital material provenance

The fine-grained detrital material that is eroded from the exposed continental surface and subsequently transported by rivers is assumed to provide a Nd isotopic composition representative of the corresponding catchment areas (Goldstein *et al.*, 2003; Bayon *et al.*, 2015). In our dataset, apart from 3 samples showing some evidence of authigenic clays that will not be considered further to discuss the evolution of the chemical weathering, all other studied clay-size fractions at Site 1259 present geochemical and petrographical features typical of a detrital origin. Isotopic geochemistry of these sediments can therefore be used to track the provenance of the upper Cretaceous sediments deposited on Demerara Rise and to reconstruct the evolution of paleoenvironments in corresponding source regions.

To constrain sediment provenance, we use the regional ε_{Nd} compilation of detrital sources published by Roddaz *et al.* (2021), applying to their published $\varepsilon_{Nd(0)}$ values the same age correction than to our own samples at 83 Ma, in order to compare them to our dataset (Fig. 1.B).

The units forming the Guiana Craton display the most unradiogenic values (Fig. 1.B). Three units can be distinguished: 1) the Archean Amapa & Imataca granitoids (AAIG), with an average $\varepsilon_{Nd(t)}$ value of -30.4 (from -41.5 to -1.5; 2σ = 17.2); 2) the Paleoproterozoic granitoids, gneiss and felsic volcanism (PGGF), with an average $\varepsilon_{Nd(t)}$ value of -22.2 (from -

365 41.5 to 30.5; 2σ = 17.2); and 3) the Paleoproterozoic high-grade granulite belts (PHGB), with
366 an average $\varepsilon_{Nd(t)}$ value of -19.8 (from -35.4 to -1.8; 2σ = 16.2). The overlying Mesoproterozoic
367 granites (MG) present an average $\varepsilon_{Nd(t)}$ value of -17.3 (from -20.0 to -14.5; 2σ = 3.9). Finally,
368 three different sources are characterized by more radiogenic values: the Greenstone Belt (GB)
369 and the Paleoproterozoic mafic intrusions (PMI) yielding values around -7.1 (from -17.6 to
370 4.3; 2σ = 13.2) and the Jurassic mafic dykes (JMD) presenting values around 1.0 (from -4.1 to
371 -6.0; 2σ = 5.9).

372 Our detrital clay $\varepsilon_{Nd(t)}$, which range between -17.5 and -14 (Figs. 3, 8) with a mean value of
373 -16.08 ± 0.91 (1σ), do not display any particular trend downcore (Table 2). They also agree
374 well with those reported by Roddaz *et al.* (2021) for a more proximal site, between about -20
375 and -13.5 (Fig. 8). The peripheral regions of the Guiana Shield bordering the Atlantic margin
376 are mainly composed of Paleoproterozoic granitoids and gneisses (PGGF; Fig. 1.B) that
377 represented the main source of the detrital material brought to Site 1259 during the late
378 Cretaceous, with a potential additional contribution of more radiogenic greenstone belts (GB)
379 (Roddaz et al., 2021).

380 The slightly more radiogenic composition of clays during the Turonian could reflect a
381 larger contribution of material derived from the greenstone belts (-7.1; Fig.1.B) or from
382 Jurassic mafic dykes (1.0 ; Fig. 1.B), which would have decreased from the Turonian to the
383 Campanian. Apart from the likely decrease in the contribution of relatively radiogenic rocks
384 to the detrital fraction deposited at Site 1259 from the Turonian to the Coniacian, and a slight
385 increase in the Maastrichtian, no major change in the source of sediments is thus depicted in
386 the Nd isotope signal.

387 The detrital fraction of the studied sediments thus mainly arises from the weathering and
388 erosion of the Guiana craton. To some extent, the evolution in relative proportions of primary
389 clay minerals (illite, chlorite) versus secondary clay minerals (smectite, kaolinite) can provide

information on tectonic uplift patterns along continental margins, as newly forming topographic reliefs naturally increase proportions of primary mineral assemblages. Indeed illite and chlorite are primary clay minerals resulting from the erosion of igneous, metamorphic and old sedimentary rocks showing limited degree of chemical weathering intensity. They typically form under relatively dry climate conditions or in active tectonic settings characterized by limited chemical weathering processes (Chamley, 1989). Under more humid climate, (semi-arid or alternation of wet and dry seasons) enhanced chemical weathering of silicate minerals typically leads to smectite formation in soils (bisialitisation ; Chamley, 1989 ; Ruffell *et al.*, 2002; Deconinck *et al*., 2019). Sub-arid or seasonally arid conditions can also favour the formation of palygorskite that precipitates in evaporative basins, such as inland seas, lakes or other peri-marine environments (Callen, 1984 ; Chamley, 1989 ; Daoudi 2004). Finally, kaolinite is commonly associated to hot and wet climate, intense chemical weathering and optimal drainage conditions (Chamley, 1989; Thiry, 2000; Ruffell *et al.,* 2002; Dera *et al*., 2009).

In northeastern South America, warm and humid conditions most likely prevailed during the late Cretaceous, as inferred from combined field data and climate model investigations (Théveniaut *et al.*, 2002 ; Hay *et al.*, 2012), coherent with the observed dominance of pedogenic smectite at the Demerara Rise. The fact that only limited amounts of kaolinite were detected during the Maastrichtian at this equatorial site raises questions. It is possible that climate was not sufficiently humid throughout the year to provide either monosialitisation or allitisation (e.g. bauxite formation) leading to abundant kaolinite-rich deposits. However, this latter hypothesis appears in contradiction with evidence of an extensive lateritization phase on the Guiana Shield during the late Cretaceous (Théveniaut *et al.*, 2002). Alternatively, the absence of kaolinite at the studied site could reflect a differential settling effect in seawater, because kaolinite grains are coarser than smectite particles (Godet *et al.*, 2008). While

kaolinite was probably formed onshore in the lateritic soils encountered on the Guiana Shield, its net export to the nearby continental margins could have been hampered by preferential deposition in the flooded shelf area (März *et al.*, 2009). Conversely, due to their smaller size, smectite was likely formed preferentially in flatter continental areas and would have been transported to more distal marine environments. Such a gradient in smectite vs kaolinite proportions due to differential settling from the continental plateau to the oceanic basins is commonly observed in modern environments (Chamley, 1989; Gingele et al., 1998).

Similarly, primary coarser clay minerals such as illite and chlorite were most likely preferentially deposited in proximal flooded shelf areas and in the GS and FOZ basins rather than on the topographic high of the Demerara Plateau (Fig. 1.B), that could explain the low proportions of primary clay minerals at the site. This would be coherent with geochemical data and sedimentary fluxes reported by März *et al.* (2009) and Loparev *et al.* (2021), indicating a sediment starvation of the Demerara Plateau at this time and preferential deposition of coarse sediments in the flooded shelf area and in the GS and FOZ basins. Such a differential setting effect, resulting in the preferential transport via surface currents of small-size smectite particles to Demerara Rise site, could explain the large dominance of smectite in studied clay fractions (85 to 100% ; Fig. 2).

Due to the very high proportions of smectite relative to other clay minerals, the variation in abundance of clay minerals must be interpreted with caution. The co-evolution of illite and palygorskite contents during the Turonian may indicate reworking of clay minerals derived from old sedimentary and igneous rocks or, alternatively, may be linked to enhanced eolian activity, as it is known that palygorskite can be easily transported by winds in sub-arid evaporitic environments (Pletsch *et al.*, 1996 ; Knidiri *et al.*, 2014). In this case, the higher palygorskite proportions recorded at Demerara Rise could indicate the existence of more arid episodes during the Turonian. Alternatively, palygorskite and illite could also come from the

440 erosion of old Mesozoic sediments derived from sedimentary basins bordering the Guiana
441 Craton, including the Takutu Basin (Fig. 1B). Indeed, palygorskite is commonly associated
442 with the Jurassic and early Cretaceous evaporitic lacustrine environments that formed during
443 the opening of the Central Atlantic (Crawford *et al.*, 1984 ; Castro *et al.*, 2021). The erosion
444 of such Mesozoic basins during the Turonian would be consistent with the pre-Coniacian
445 catchment areas defined by Roddaz *et al.* (2021) based on ε_{Nd} and trace element abundances.
446 In any case, these minerals represent a very low proportion of the total clay content that is
447 mainly dominated by detrital contemporaneous smectites and should not impact Nd-Hf
448 isotopic values.

449 During the Turonian, the higher content of palygorskite and illite, if eroded from old
450 Mesozoic sediments, could be indicative of higher erosion rates. A slight increase in illite
451 proportions is also recorded during the Coniacian-Campanian interval, with a maximum value
452 around 80 Ma ago, coupled with slightly higher feldspar contents in the bulk sediment (Fig.
453 2). This is also illustrated by the variations of the (I+C)/S and Feld/Clays ratio in figure 8.
454 Although discrete, these features may reflect enhanced mechanical erosion promoting both
455 primary silicate minerals (e.g. feldspar ; Figs. 2, 8) and coarse and primary clay minerals (e.g.
456 illite) during an uplift phase. This would be consistent with the timing of the main pulses of
457 tectonic activity and higher sedimentation rates in the GS and FOZ basins during this interval
458 (Sapin *et al.*, 2016 ; Loparev *et al.*, 2020 ; Fig. 1.B). Presumably, at that time, enhanced
459 tectonic activity along the northeastern South American margin was accompanied by
460 enhanced erosional fluxes and nutrient export to seawater, which could also have driven
461 enhanced biosiliceous marine productivity inferred from the (O+C)/Ca ratio (Fig. 8). This
462 mechanism may explain the concomitant increase of biogenic phases and the detrital input
463 during the Campanian in relation to the main tectonic pulse, although a role of aerial

464 explosive volcanism activity as a potential source of siliceous material cannot be excluded
465 (Frogner *et al.*, 2001 ; Stokke *et al.*, 2021).
466
467 5.3. Evolution of chemical weathering linked to climate and tectonic.
468 The identification of distinct uplift pulses during the Turonian and Campanian-to-early
469 Maastrichtian period in the studied area (Fig. 9, Sapin *et al.*, 2016) has provided evidence for
470 a major tectonic phase affecting the eastern South American margin at that time. Argon/argon
471 (Ar/Ar) dating of the late Cretaceous planation surface S0 (McConnell, 1968 ; Sapin *et al.*,
472 2016) yields an age of 71 Ma, while apatite fission track data (AFTA) indicate ages of 77 ± 3
473 Ma, 83 ± 5 Ma and 99 ± 9 Ma for the periods of enhanced regional tectonic activity (Fig. 9 ;
474 Sapin *et al.*, 2016). In the FOZ basin, the highest terrigenous accumulation rates occurred
475 during the Campanian-Maastrichtian interval (Loparev *et al.*, 2021), associated with the main
476 uplift phase, while in the GS basin, Roddaz et al. (2021) shows an increase in sedimentation
477 rates during the Santonian.

478 In order to track the impact of tectonic uplift, inferred from Ar/Ar dating of planation
479 surfaces and AFTA, on the evolution of chemical weathering intensity in NE South America,
480 we now consider Nd and Hf isotope data measured in the clay-size fraction. The combined
481 use of Nd and Hf isotopes in fine-grained sediment records is a powerful proxy to track
482 changes in continental chemical weathering (Bayon *et al.*, 2012 ; Fontanier *et al.*, 2018 ;
483 Corentin *et al.*, 2022; Bayon et al., 2022). While the Lu-Hf and Sm-Nd isotopic systems
484 behave similarly during magmatic processes, defining a so-called «Terrestrial array» in most
485 igneous and sedimentary rocks (Fig. 6; Vervoort *et al.*, 1999 ; Vervoort *et al.*, 2011), they are
486 decoupled during Earth surface processes such as chemical weathering and sediment transport
487 (Vervoort *et al.*, 1999 ; Bayon *et al.*, 2016 ; Garçon *et al.*, 2013 ; Garçon & Chauvel, 2014 ;
488 Chauvel *et al.*, 2014). This decoupling is partly due to mineral sorting, which causes

preferential enrichment of zircons in the coarse-grained sediment fraction, characterized by high Hf concentrations and very low ε_{Hf} (unradiogenic) compositions (Vervoort *et al.*, 1999 ; Chauvel *et al.*, 2014). By contrast, clay-size fractions of sorted sediments are typically depleted in zircons and hence are systematically shifted towards more radiogenic ε_{Hf} values compared to coarser sediment fractions, defining a so-called « clay array » (Zhao et al., 2014; Bayon *et al.*, 2016 ; Fig. 6). Additionally, the mineral phases most susceptible to chemical weathering on continents are typically enriched in Lu relative to Hf, hence leading to the preferential release of radiogenic Hf during weathering (Bayon *et al.*, 2006 ; Bayon *et al.*, 2016 ; Dausmann *et al.*, 2019). Upon formation of secondary clay minerals in soils, a fraction of dissolved radiogenic Hf can be incorporated into clays (Bayon *et al.*, 2016). As a result, clay-size fractions derived from intensively weathered soils are associated with more radiogenic clay ε_{Hf} signatures, which partly reflect an increase in the relative proportion of secondary clay minerals (high ε_{Hf}) relative to unweathered primary detrital mineral (low ε_{Hf}). In fine-grained sediment records, a more intense chemical silicate weathering hence results in a vertical departure of clay ε_{Hf} from the « clay array », noted $\Delta\varepsilon_{Hf}$ (Fig. 6 ; Bayon *et al.*, 2016). Note that $\Delta\varepsilon_{Hf}$ has not been calculated for the 3 samples presenting evidence of a seawater imprint on the clay fraction Nd isotope signal linked to the presence of authigenic clays.

The analysed clay fraction presents low zirconium (Zr) concentrations (between 42 and 157 ppm), in the range of modern clay-size fractions separated from river sediments (Bayon *et al.*, 2015). Additionally, there is no significant correlation between ε_{Hf} values and Zr concentrations ($R^2 = 0.23$; Supplementary Fig. 1), nor between $\Delta\varepsilon_{Hf}$ and Zr concentrations. This observation indicates that the $\Delta\varepsilon_{Hf(t)clay}$ evolution of studied clays is not controlled by the presence of residual zircons in the isolated < 2µm sediment fraction, but rather reflects variations in silicate weathering intensity of the catchment area.

514 The close correspondence of $\Delta\varepsilon_{Hf\ clay}$ with climatic parameters and with the chemical index
515 of alteration (CIA) observed in clays recovered from rivers receiving weathering products
516 from source rocks of various nature suggests a minor influence of lithology on $\Delta\varepsilon_{Hf}$ (Bayon *et*
517 *al.*, 2016). At Site 1259, the limited $\varepsilon_{Nd(t)}$ variations through the studied interval points to the
518 absence of major change in the lithologies of the sediment source, while $\Delta\varepsilon_{Hf(t)clay}$ increases
519 quite markedly. Most importantly, no correlation is depicted between $\varepsilon_{Nd(t)}$ and $\Delta\varepsilon_{Hf(t)}$,
520 demonstrating that variations in $\Delta\varepsilon_{Hf(t)}$ are not controlled by lithology variations of the source
521 rock at this site (Supplementary figure 2).
522 Calculated $\Delta\varepsilon_{Hf(t)clay}$ values at Demerara Rise are thus interpreted hereafter to reflect the
523 evolution of chemical weathering intensity, with the depicted decrease in $\Delta\varepsilon_{Hf(t)clay}$ pointing
524 to a decrease in weathering of surrounding catchment regions from the end of the Turonian to
525 the Santonian or beginning of Campanian (Fig. 8 ; Bayon *et al.*, 2016). Then, from
526 Campanian to the end of Maastrichtian, a marked increase in regional silicate weathering
527 intensity is recorded (Figs. 3, 8). Superimposed on this trend, a slight decrease in $\Delta\varepsilon_{Hf(t)clay}$
528 values, reflecting an interval of lower weathering intensity, is also recorded during the late
529 Campanian and Early Maastrichtian, of about 2.0 (Figs. 3, 8).

530 The Chemical Index of Alteration (CIA) has also been widely used to track changes in
531 chemical weathering (e.g. Young & Nesbitt, 1999; Roddaz et al., 2006), as it provides an
532 estimation of the degree of mobile element depletion relative to immobile elements during
533 chemical weathering (Nesbitt & Young, 1982), although this proxy is known to be influenced
534 by sediment source and mineral sorting (Fantasia *et al.*, 2019). At Site 1259, no major change
535 in sediment provenance occurred during the late Cretaceous but Campanian sediments are
536 marked by higher opal-CT and quartz contents increasing the concentrations of silicon and
537 thus decreasing aluminium relative proportions. The CIA value calculated for the two samples
538 exhibiting the highest contents of biogenic minerals is very low (<50), hence suggesting a

539 dilution effect by Si impeding its use as a weathering proxy in the interval marked by high
540 opal-CT and quartz contents (Fig. 8). The pronounced increase of the CIA that subsequently
541 follows (from 56 to 74) is however not associated to concomitant change in opal-CT and
542 quartz contents, nor in sediment sources as ε_{Nd} values remain quite constant, and thus could
543 reflect an increase of chemical weathering intensity from the middle Campanian to the late
544 Maastrichtian. This interpretation would be in agreement with the increase depicted in
545 $\Delta\varepsilon_{Hf(t)clay}$.

546 Over long timescales, the evolution of continental chemical weathering is thought to be
547 driven mostly by climate and tectonics. Increasing temperature and precipitation favour the
548 kinetics of silicate weathering reactions and increase wetting of reactive mineral surface areas,
549 enhancing silicate mineral dissolution rates (White & Blum, 1995 ; Berner *et al.*, 1983 ;
550 Gaillardet *et al.*, 1999 ; Barron & Washington, 1985 ; Pierrehumbert, 2002). Active tectonic
551 settings associated with high denudation rates and mechanical erosion can also promote high
552 chemical weathering rates by favouring both the disaggregation of silicate minerals and
553 renewing the exposure of fresh rock surfaces available to weathering. The relationship
554 between mechanical erosion and chemical weathering is however not straightforward. Under
555 supply-limited weathering conditions, the rate of chemical weathering is proportionally
556 related to denudation rates (Raymo *et al.*, 1988 ; West *et al.*, 2005 ; Gabet & Mudd, 2009). In
557 contrast, under kinetically-limited weathering conditions, detrital material is removed too fast
558 from the regolith, and higher denudation rates are not accompanied by higher chemical
559 weathering rates (West, 2005 ; Gabet and Mudd, 2009).

560 The evolution of chemical weathering intensity depicted by $\Delta\varepsilon_{Hf(t)clay}$ matches relatively
561 well the evolution of ocean temperature inferred from both planktic foraminifera at Demerara
562 Rise (Fig. 8 ; Bornemann *et al.*, 2008) and the global benthic foraminiferal $\delta^{18}O$
563 reconstruction (Fig. 8 ; Friedrich *et al.*, 2012). Chemical weathering in northeastern South

America markedly decreased during the climate cooling recorded from the end of the Turonian to the early Campanian, suggesting a climatic control of this evolution, as lower temperature reduces silicate weathering reactions (Fig. 8 ; White and Blum, 1995). Similarly, the cooling recorded in the latest Campanian and early Maastrichtian appears to be also associated with a decrease, albeit more limited, of continental weathering intensity (Fig. 8). However, if a slight warming is observed in the foraminiferal $\delta^{18}O$ dataset during the middle and late Campanian, global temperature remains markedly lower in the late Campanian and Maastrichtian than during the Turonian, when chemical weathering markedly increased as inferred from $\Delta\varepsilon_{Hf(t)clay}$ values exceeding those recorded for the Turonian. Therefore, for the middle Campanian to Maastrichtian interval, the evolution of global temperature is unlikely to fully account for our chemical weathering record, hence requiring an additional process resulting in enhanced silicate weathering. Throughout the studied interval, there is no evidence for marked changes in the amount of precipitation; nearby continental regions remained within a humid climatic belt as documented by the occurrence of laterites and bauxites throughout the late Cretaceous (Théveniaut *et al.*, 2002 ; Hay, 2012). Consequently, we infer that the observed marked increase in chemical weathering was presumably not induced by a regional climate shift towards wetter conditions.

As mentioned above, during the Campanian, the northeastern South American margin experienced several tectonic pulses that led to the uplift of the craton (McConnell, 1968 ; Potter, 1997 ; Harman *et al*. 1998 ; Morais Neto et al. 2009 ; Peulvast and Bétard 2015 ; Sapin *et al.*, 2016 ; Monteiro *et al*. 2018). This uplift most likely drove enhanced mechanical erosion as suggested by the slight increase in illite and feldspar at Site 1259, which, in a permanently humid climatic belt, could have been associated with more intense silicate weathering as well (West, 2005 ; Gabet & Mudd, 2009). The occurrence of a major uplift phase concomitant with a pronounced $\Delta\varepsilon_{Hf(t)clay}$ increase (Fig. 8), with values exceeding those recorded in the Turonian

589 despite markedly lower temperatures, strongly points towards tectonics as being the main
590 driver of chemical weathering variability in northeastern South America during the middle
591 Campanian to Maastrichtian interval. By contrast, from the end of the Turonian to the early
592 Campanian interval, when tectonic activity was reduced, climate was instead the main
593 parameter controlling the evolution of chemical weathering in the study area.

594 Altogether, our data thus suggest the dominant control of tectonics on continental
595 weathering when occurring under wet climate conditions, with a more limited role of
596 temperature. These findings complement previous inferences based on Site 356 offshore
597 Brazil, which showed that under semi-arid climate conditions, chemical weathering did not
598 respond to the tectonic uplift of the Brazilian margin until local climate evolved toward more
599 hydrolysing conditions (Corentin *et al.*, 2022). Surprisingly, the $\Delta\varepsilon_{Hf(t)clay}$ values recorded at
600 site 1259 are negative for the most part, with values down to -5 which are observed at present
601 in cold and dry climatic zones, although values recorded during the latest Campanian and
602 Maastrichtian, up to 1, are observed in modern tropical humid belts (Bayon et al. (2016). By
603 contrast, higher $\Delta\varepsilon_{Hf(t)clay}$ values are recorded at site 356 located in a semi-arid climatic zone
604 (Fig. 6). This apparent discrepancy may further point to a preponderant role of tectonics on
605 silicate weathering through supply of fresh minerals exposed to weathering processes,
606 favoured by enhanced physical erosion. At site 1259, in the context of relative tectonic
607 quiescence during the interval recording the most negative values, these low $\Delta\varepsilon_{Hf(t)clay}$ values
608 may reflect the existence of limited chemical weathering under supply-limited conditions
609 (West et al., 2005; Gabet and Mudd, 2009), impeded by low physical erosion rates reducing
610 the renewed supply of fresh minerals to weathering processes. Alternatively, the
611 correspondence between absolute $\Delta\varepsilon_{Hf(t)clay}$ values with climatic zones may have been
612 different in the overall greenhouse climate mode of the late Cretaceous than from our modern
613 icehouse climate mode, in which they have been established. Although the significance of

614 absolute $\Delta\varepsilon_{Hf(t)clay}$ values still needs further investigation, our study highlights the potential of
615 relative variations in $\Delta\varepsilon_{Hf(t)clay}$ at a specific site remains to infer relative changes in silicate
616 chemical weathering at a local scale.

617 Variations in continental weathering can also impact global climate through atmospheric
618 CO_2 drawdown by silicate weathering reactions. Combined Hf-Nd and clay mineralogical
619 data from Site 356 offshore Brazil have recently highlighted an increase in silicate weathering
620 along the Brazilian margin from the Santonian onward, which coincided with an acceleration
621 of the late Cretaceous global climate cooling (Friedrich *et al*., 2012). At Site 1259, the marked
622 increase in chemical weathering affecting the northeastern South American margin initiated
623 during the middle Campanian, appears post-dating the main global cooling phase inferred
624 from the benthic foraminiferal $\delta^{18}O$ record. While the tectonic uplift of the northern South
625 American margin and its impact on chemical weathering hence could not have triggered the
626 long-term climate cooling during the late Cretaceous, it is possible that weathering-driven
627 atmospheric CO_2 drawdown contributed to maintaining cooler conditions in the late
628 Campanian and Maastrichtian. Altogether, the data from Site 356 (Corentin *et al*., 2022)
629 offshore southeastern Brazil, and the new data from Site 1259 at Demerara Rise (this study)
630 highlight the possible importance of the late Cretaceous uplift of the Eastern South American
631 margin on the long-term cooling recorded during this period.

632

633 *Conclusion*

634 The new $\Delta\varepsilon_{Hf(t)clay}$ proxy based on combined Nd-Hf isotope measurements of clay-size
635 fractions was applied to a sediment record from Demerara Rise in order to the reconstruct the
636 evolution of continental silicate weathering intensity at the northeastern South American
637 margin during the late Cretaceous.

638 The depicted evolution of $\Delta\varepsilon_{Hf(t)clay}$ seems to show a co-variation of chemical weathering
639 with global climate, except during the middle Campanian to Maastrichtian interval when
640 inferred chemical weathering intensity was higher than during the Turonian despite cooler
641 climate conditions. During this Campanian-to-Maastrichtian period, our proxy record
642 indicates that major tectonic uplift of the northeastern South American margin was
643 accompanied by an intensification of chemical weathering. By contrast, from the end of the
644 Turonian to the early Campanian, i.e. a period characterized by reduced tectonic activity, the
645 evolution of continental weathering in northern South America was mostly influenced by
646 climate.
647 Our dataset brings new constraints on the combined influence of tectonics and climate in
648 driving the long-term evolution of continental chemical weathering through time. Under
649 persistent tropical climate conditions, tectonics appears to play a major role in controlling
650 silicate weathering, while the impact of temperature appears less prominent. Overall, the
651 response of chemical weathering to tectonic uplift along the eastern margin of South America
652 inferred from our proxy data suggests that this major tectonic event could have partially
653 contributed to the late Cretaceous cooling through weathering-driven atmospheric CO_2
654 drawdown.

655

656 *Data availability*

657 All the data are provided in the supplementary materials attached to this paper.

658

659 *Acknowledgments*

660 We thank IODP for providing access the material. IODP France and ANR RISE funded the
661 project. We also thank Rémi Chassagnon (Laboratory ICB, University of Burgundy) and

662 INRAe of Dijon, Ludovic Bruneau of the Biogéosciences Laboratory and GISMO analytical
663 Platform (University of Burgundy), Marie-Laure Rouget and Bleuenn Gueguen of the Pôle
664 Spectrométrie Océan (Brest) and Philippe Telouk of the ENS Lyon for their analytical
665 support.

666

667 *References*

668 Barrat, J.A., Keller, F., Amossé, J., Taylor, R.N., Nesbitt, R.W., Hirata, T. 1996. Determination
669 of Rare Earth Elements in Sixteen Silicate Reference Samples by Icp-Ms After Tm Addi-
670 tion and Ion Exchange Separation. Geostandards Newsletter 20, 133–139.

671 Barron, E. J., Washington, W. M. 1985. Warm Cretaceous climates: High atmospheric CO_2 as a
672 plausible mechanism. In: The carbon cycle and atmospheric CO_2 : Natural Variations,
673 Archean To present (Geophys Monogr. 32) AGU, edited by Sundquist, E. and Broeker,
674 W., 546–553, Washington DC, 984-999.

675 Basile, C., Maillard, A., Patriat, M., Gaullier, V., Loncke, L., Roest, W., Mercier de Lépinay,
676 M., Pattier, F. 2013. Structure and Evolution of the Demerara Plateau, Offshore French
677 Guiana: Rifting, Tectonic Inversion and Post-Rift Tilting at Transform-Divergent Margins
678 Intersection. Tectonophysics, Basin Dynamics, 591 (April): 16-29.

679 Bayon, G., German, C.R., Boella, R.M., Milton, J.A., Taylor, R.N., Nesbitt, R.W. 2002. An
680 improved method for extracting marine sediment fractions and its application to Sr and Nd
681 isotopic analysis. Chemical Geology 187, 179–199.

682 Bayon, G., Vigier, N., Burton, K.W., Agnès Brenot, J.C., Etoubleau, J., Chu, N.-C. 2006. The
683 control of weathering processes on riverine and seawater hafnium isotope ratios. Geology
684 34, 433–436.

685 Bayon, G., Barrat, J.A., Etoubleau, J., Benoit, M., Bollinger, C., Révillon, S. 2009b.
686 Determination of Rare Earth Elements, Sc, Y, Zr, Ba, Hf and Th in Geological Samples by
687 ICP-MS after Tm Addition and Alkaline Fusion. Geostandards and Geoanalytical Research
688 33, 51–62.

689 Bayon, G., Dennielou, B., Etoubleau, J., Ponzevera, E., Toucanne, S., Bermell, S. 2012. Inten-
690 sifying Weathering and Land Use in Iron Age Central Africa. Science 335, 1219–1222.

691 Bayon, G., Toucanne, S., Skonieczny, C., André, L., Bermell, S., Cheron, S., ... & Barrat, J. A.
692 (2015). Rare earth elements and neodymium isotopes in world river sediments revisited.
693 *Geochimica et Cosmochimica Acta*, *170*, 17-38.

694 Bayon, G., Skonieczny, C., Delvigne, C., Toucanne, S., Bermell, S., Ponzevera, E., André, L.
695 2016. Environmental Hf–Nd isotopic decoupling in World river clays. Earth and Planetary
696 Science Letters 438, 25–36.

697 Bayon, G., Bindeman, I. N., Trinquier, A., Retallack, G. J., & Bekker, A. (2022). Long-term
698 evolution of terrestrial weathering and its link to Earth's oxygenation. *Earth and Planetary*
699 *Science Letters*, *584*, 117490.

700 Berner, R. A., Lasaga, A. C., Garrels, R. M. 1983. The carbonate-silicate geochemical cycle
701 and its effect on atmospheric carbon dioxide over the past 100 million years, Am. J. Sci.
702 283, 641-683.

703 Bornemann, A., Norris, R. D., Friedrich, O., Beckmann, B., Schouten, S., Damsté, J. S. S.,
704 Vogel, J., Hofmann, P., Wagner, T. 2008. Isotopic Evidence for Glaciation During the
705 Cretaceous Supergreenhouse. Science 319, 189-192.

706 Bouvier, A., Vervoort, J.D., Patchett, P.J. 2008. The Lu–Hf and Sm–Nd isotopic composition
707 of CHUR: Constraints from unequilibrated chondrites and implications for the bulk
708 composition of terrestrial planets. Earth and Planetary Science Letters 273, 48–57.

709 Callen, R.A. 1984. Clays of the palygorskite-sepiolite group: Depositional environment, age
710 and distribution. In Singer, A., Galan, E. (Eds.) Palygorskite-sepiolite occurrences, genesis
711 and uses. Dev. Sedimentol. 37. Elsevier Sci. Publ. Co., Amsterdam, 1-37.

712 Castro, R., Giorgioni, M., de Souza, V., Ramos, M., Feitoza, L. M., Dino, R., Antonioli, L.
713 2021. Facies analysis, petrography, and palynology of the Pirara Formation (Upper Ju-
714 rassic-Lower Cretaceous) - Tacutu Basin (Roraima, Brazil). Journal of South American
715 Earth Sciences 112, 103574.

716 Chamley, H. 1989. Clay sedimentology ed. Springer-Verlag Berlin Heidelberg GmbH.

717 Chauvel, C., Garçon, M., Bureau, S., Besnault, A., Jahn, B., Ding, Z. 2014. Constraints from
718 loess on the Hf–Nd isotopic composition of the upper continental crust. Earth and Plane-
719 tary Science Letters 388, 48–58.

720 Chu, N.-C., Taylor, R.N., Chavagnac, V., Nesbitt, R.W., Boella, R.M., Milton, J.A., German,
721 C.R., Bayon, G., Burton, K. 2002. Hf isotope ratio analysis using multi-collector induc-
722 tively coupled plasma mass spectrometry: an evaluation of isobaric interference correc-
723 tions. J. Anal. At. Spectrom. 17, 1567–1574.

724 Clauer, N., O'Neil, J.R., Bonnot-Courtois, C., Holtzapffel, T. 1990. Morphological, Chemical,
725 and Isotopic Evidence for an Early Diagenetic Evolution of Detrital Smectite in Marine
726 Sediments. Clays Clay Miner. 38, 33–46.

727 Corentin, P., Pucéat, E., Pellenard, P., Freslon, N., Guiraud, M., Blondet, J., Adatte, T., Bayon,
728 G. 2022. Hafnium-neodymium isotope evidence for enhanced weathering and uplift-cli-
729 mate interactions during the Late Cretaceous. Chemical Geology 591, 12074.

730 Crawford, F.D., Szelewski, C.E., Alvey, G.D. 1984. Geology and exploration in the Takutu
731 graben of Guyana. J. Pet. Geol. Beaconsfield, 8 (1), 5-36.

732 Cullers, R. L. 2000. The Geochemistry of Shales, Siltstones and Sandstones of Pennsylvanian
733 Permian Age, Colorado, USA: Implications for Provenance and Metamorphic Studies.
734 Lithos 51 (March): 181-203.

735 Daoudi, L. 2004. Palygorskite in the uppermost Cretaceous–Eocene rocks from Marrakech
736 High Atlas, Morocco. Journal of African Earth Sciences, Key Points on African Geology
737 39, 353–358.

738 Dausmann, V., Gutjahr, M., Frank, M., Kouzmanov, K., Schaltegger, U. 2019. Experimental
739 evidence for mineral-controlled release of radiogenic Nd, Hf and Pb isotopes from granitic
740 rocks during progressive chemical weathering. Chemical Geology, 507, 64-84.

741 Deconinck, J. F., Hesselbo, S. P., Pellenard, P. 2019. Climatic and sea level control of Jurassic
742 (Pliensbachian) clay mineral sedimentation in the Cardigan Bay Basin, Llanbedr (Mochras
743 Farm) borehole, Wales. Sedimentology 66 (7), 2769-2783.

744 Dera, G., Pellenard, P., Neige., P., Deconinck, J. F., Pucéat, E., Dommergues, J. L. 2009.
745 Distribution of clay minerals in Early Jurassic Peritethyan seas : palaeoclimatic
746 significance inferred from multiproxy comparisons. Palaeogeography, Palaeoclimatology,
747 Palaeoecology 271 (1-2), 39-51.Engelmann de Oliveira, C.H., Jelinek, A.R., Chemale, F.,
748 Cupertino, J.A. 2016. Thermotectonic history of the southeastern Brazilian margin:
749 Evidence from apatite fission track data of the offshore Santos Basin and continental
750 basement. Tectonophysics 685, 21–34.

751 Erbacher, J., Mosher, D.C., Malone, M.J. 2004. Shipboard scientific party. Proc. ODP. In. Re-
752 ports, vol. 207.

753 Erbacher, J., Friedrich, O., Wilson, P.A., Birch, H., Mutterlose, J. 2005. Stable organic carbon
754 isotope stratigraphy across Oceanic Anoxic Event 2 of Demerara Rise, western tropical
755 Atlantic. Geochem. Geophys. Geosyst. 6, Q06010.

756 Fagel, N., André, L., Chamley, H., Debrabant, P., Jolivet, L. 1992. Clay sedimentation in the
757 Japan Sea since the Early Miocene: influence of source-rock and hydrothermal activity.
758 Sedimentary Geology 80, 27–40.

759 Fantasia, A., Adatte, T., Spangenberg, J.E., Font, E., Duarte, L.V., Föllmi, K.B. 2019. Global
760 versus local processes during the Pliensbachian–Toarcian transition at the Peniche GSSP,
761 Portugal: A multi-proxy record. Earth-Science Reviews 198, 102932.

762 Fontanier, C., Mamo, B., Toucanne, S., Bayon, G., Schmidt, S., Deflandre, B., Dennielou, B.,
763 Jouet, G., Garnier, E., Sakai, S., Lamas Ruth, M., Duros, P., Toyofuku, T., Salé, A., Belle-
764 ney, D., Bichon, S., Boissier, A., Chéron, S., Pitel, M., Roubi, A., Rovere, M., Grémare,
765 A., Dupré, S., Jorry, S. 2018. Are deep-sea ecosystems surrounding Madagascar threatened
766 by land-use or climate change? Deep Sea Research Part I: Oceanographic Research Papers
767 131, 93-100.

768 Frank, M., 2002. Radiogenic Isotopes: Tracers of Past Ocean Circulation and Erosional Input.
769 Reviews of Geophysics 40, 1-38.

770 Friedrich, O., Erbacher, J. 2006. Benthic foraminiferal assemblages from Demerara Rise (ODP
771 Leg 207, western tropical Atlantic): Possible evidence for a progressive opening of the
772 Equatorial Atlantic Gateway: Cretaceous Research 27, 377–397.

773 Friedrich, O., Norris, R.D., Erbacher, J. 2012. Evolution of middle to Late Cretaceous oceans
774 — A 55 m.y. record of Earth's temperature and carbon cycle. Geology 40, 107–110.

775 Frogner, P., Gíslason, S. R., Oskarsson, N. 2001. Fertilizing potential of volcanic ash in ocean
776 surface water. Geology 29 (6), 487-490.

777 Gabet, E.J., Mudd, S.M. 2009. A theoretical model coupling chemical weathering rates with
778 denudation rates. Geology 37, 151–154.

779 Gaillardet, J., Dupré, B., Louvat, P., Allègre, C.J. 1999. Global silicate weathering and CO_2
780 consumption rates deduced from the chemistry of large rivers. Chemical Geology. 159, 3–
781 30.

782 Gallagher, K., Brown, R. 1999. The Mesozoic denudation history of the Atlantic margins of
783 southern Africa and southeast Brazil and the relationship to offshore sedimentation. Geo-
784 logical Society, London, Special Publications 153, 41–53.

785 Garçon, M., Chauvel, C., France-Lanord, C., Huyghe, P., Lavé, J. 2013. Continental sedimen-
786 tary processes decouple Nd and Hf isotopes. Geochim. Cosmochim. Acta 121, 177–195.

787 Garçon, M., Chauvel, C. 2014. Where is basalt in river sediments, and why does it matter? Ear-
788 th and Planetary Science Letters 407, 61-69.

789 Gingele, F. X., Müller, P. M., & Schneider, R. R. (1998). Orbital forcing of freshwater input in
790 the Zaire Fan area—clay mineral evidence from the last 200 kyr. *Palaeogeography,*
791 *Palaeoclimatology, Palaeoecology*, *138*(1-4), 17-26.

792 Godet, A., Bodin, S., Adatte, T., Föllmi, K.B. 2008. Platform-induced clay–mineral fractiona-
793 tion along a northern Tethyan basin–platform transect: implications for the interpretation
794 of Early Cretaceous climate change (Late Hauterivian–Early Aptian). Cret. Res. 29, 830–
795 847.

796 Goldstein, S.L., Hemming, S.H. 2003. Long lived isotopic tracers in oceanography,
797 paleoceanography, and ice sheet dynamics. In: Elderfield, H., Turekian, K.K. 2003 (Eds.),
798 Treatise on Geochemistry. Elsevier, New York, 453–489.

799 Gradstein, F.M., Ogg, J.G., Schmitz, M.D., Ogg, G.M. 2012. The Geologic Time Scale 2012.
800 Elsevier.

801 Green, P.F., Duddy, I.R., Japsen, P., Bonow, J.M., Malan, J.A. 2017. Post-breakup burial and
802 exhumation of the southern margin of Africa. Basin Research 29, 96-127.

803 Green, P.F., Japsen, P., Chamlers, J.A., Bonow, J.M., Duddy, I.R. 2018. Gondwana Research
804 53, 58- 81.

805 Haq, B.U. 2014. Cretaceous eustasy revisited. Global and Planetary Change 113, 44-58.

806 Harman, R., Gallagher, K., Brown, R., Raza, A., Bizzi, L. 1998. Accelerated denudation and
807 tectonic/geomorphic reactivation of the cratons of northeastern Brazil during the Late
808 Cretaceous. Journal of Geophysical Research 103, 27,091– 27,105.

809 Hay, W.W., Floegel, S. 2012. New thoughts about the Cretaceous climate and oceans. Earth
810 Sci. Rev. 115, 262–272.

811 Hesse, R. 1988. Diagenesis# 13. Origin of chert: Diagenesis of biogenic siliceous sediments.
812 *Geoscience Canada*, 15(3), 171-192.

813 Japsen, P., Bonow, J.M., Green, P.F., Cobbold, P. R., Chiossi, D., Lilletveit, R., Magnavita,
814 L.P., Pedreira, A. 2012. Episodic burial and exhumation in NE Brazil after opening of the
815 South Atlantic. GSA Bulletin 124, 800-816.

816 Jochum, K. P., Weis, U., Schwager, B., Stoll, B., Wilson, S. A., Haug, G. H., Andreae, M. O.,
817 Enzweiler, J. 2016. Reference values following ISO guidelines for frequently requested
818 rock reference materials. Geostandards and Geoanalytical Research, 40 (3), 333-350.

819 Karpoff, A.M., Destrigneville, C., Stille, P. 2007. Clinoptilolite as a new proxy of enhanced
820 biogenic silica productivity in lower Miocene carbonate sediments of the Bahamas plat-
821 form : isotopic and thermodynamic evidence. Chem. Geol., 245, 285–304.

822 Knidiri, A., Daoudi, L., El Ouahabi, M., Rhouta, B., Rocha, F., Fagel, N. 2014. Palaeogeogra-
823 phic controls on palygorskite occurrence in Maastrichtian-Palaeogene sediments of the
824 Western High Atlas and Meseta Basins (Morocco). Clay Minerals 49 (4), 595-608.

825 Loncke, L., Roest, W. R., Klingelhoefer, F., Basile, C., Graindorge, D., Heuret, A., Marcaillou,
826 B., Museur, T., Fanget, A. S., Mercier de Lépina, M. 2020. Transform Marginal Plateaus.
827 Earth-Science Reviews 203 (April): 102940.

828 Loparev, A., Rouby, D., Chardon, D., Dall'Asta, M., Sapin, F., Bajolet, F., et al. (2021).
829 Superimposed rifting at the junction of the Central and Equatorial Atlantic: Formation of
830 the passive margin of the Guiana Shield. *Tectonics*, *40*, e2020TC006159.

831 Lugmair, G.W., Marti, K. 1977. Sm-Nd-Pu timepieces in the Angra dos Reis meteorite. Earth
832 and Planetary Science Letters 35, 273–284.

833 Martin, E. E., MacLeod, K. G., Jiménez Berrocoso, A., Bourbon, E. 2012. Water Mass
834 Circulation on Demerara Rise during the Late Cretaceous Based on Nd Isotopes. Earth and
835 Planetary Science Letters 327-328 (April): 111-20.

836 März, C., Beckmann, B., Franke, C., Vogt, C., Wagner, T., Kasten, S. 2009. Geochemical envi-
837 ronment of the Coniacian–Santonian western tropical Atlantic at Demerara Rise. Palaeo-
838 geography, Palaeoclimatology, Palaeoecology 273, 286-301.

839 McConnell, R.B. 1968. Planation Surfaces in Guyana. The Geographical Journal 134, 506–520.

840 McLennan, S.M. 1993. Weathering and Global Denudation. The Journal of Geology 101, 295–
841 303.

842 Monteiro, H. S., Vasconcelos, P. M. P., Farley, K. A., Lopes, C. A. M. 2018. Age and
843 Evolution of Diachronous Erosion Surfaces in the Amazon: Combining (U-Th)/He and
844 Cosmogenic ^{3}He Records. Geochimica et Cosmochimica Acta 229 (May): 162-83.

845 Moore, D.M., Reynolds, R.C. 1989. X-ray diffraction and the identification and analysis of clay
846 minerals. X-ray diffraction and the identification and analysis of clay minerals.

847 Morais Neto, J.M., Hegarty, K.A., Karner, G.D., Alkmim, F.F. 2009. Timing and mechanisms
848 for the generation and modification of the anomalous topography of the Borborema Pro-
849 vince, northeastern Brazil. Marine and Petroleum Geology 26, 1070-1086.

850 Mourlot, Y., Roddaz M., Dera, G., Calvès, G., Kim, J.-H., Chaboureau, A.-C., Mounic, S.,
851 Raisson, F. 2018. Geochemical Evidence for Large-Scale Drainage Reorganization in
852 Northwest Africa During the Cretaceous. Geochemistry, Geophysics, Geosystems, 1690-
853 1712.

854 Nederbragt, A.J., Thurow, J., Pearce, R. 2007. Sediment composition and cyclicity in the Mid-
855 Cretaceous at Demerara Rise, ODP Leg 207. In: Mosher, D.C., Erbacher, J., Malone, M.J.,
856 et al. (Eds.), Proc. ODP Sci. Results 207, 1–31.

857 Nesbitt, H.W., Young, G.M. 1982. Early Proterozoic climates and plate motions inferred from
858 major element chemistry of lutites. Nature 299, 715–717.

859 O'Brien, C.L., Robinson, S.A., Pancost, R.D., Sinninghe Damsté, J.S., Schouten, S., Lunt, D.J.,
860 Alsenz, H., Bornemann, A., Bottini, C., Brassell, S.C., Farnsworth, A., Forster, A., Huber,
861 B.T., Inglis, G.N., Jenkyns, H.C., Linnert, C., Littler, K., Markwick, P., McAnena, A.,
862 Mutterlose, J., Naafs, B.D.A., Püttmann, W., Sluijs, A., van Helmond, N.A.G.M., Velle-
863 koop, J., Wagner, T., Wrobel, N.E. 2017. Cretaceous sea-surface temperature evolution:
864 Constraints from TEX86 and planktonic foraminiferal oxygen isotopes. Earth-Science
865 Reviews 172, 224–247.

866 Petschick, R. 2001. MacDiff. Freeware scientific graphical analysis software for X-ray diffrac-
867 tion profiles. Frankfurt, Germany.

868 Peulvast, J.-P., Bétard, F. 2015. A History of Basin Inversion, Scarp Retreat and Shallow
869 Denudation: The Araripe Basin as a Keystone for Understanding Long-Term Landscape
870 Evolution in NE Brazil." Geomorphology, Patterns and rates of Cenozoic landscape
871 change in orogenic and post-orogenic settings, 233 (March): 20-40.

872 Pierrehumbert, R.T. 2002. The hydrologic cycle in deep-time climate problems. Nature 419,
873 191-198.

874 Pletsch, T., Daudi, L., Chamley, H., Deconinck, J.F., Charroud, M. 1996. Palaeogeographic
875 controls on palygorskite occurrence in mid-Cretaceous sediments of Morocco and adjacent
876 basins. Clay Minerals 31, 403-416.

877 Potter, P. E. 1997. The Mesozoic and Cenozoic Paleodrainage of South America: A Natural
878 History. Journal of South American Earth Sciences 10 (5): 331-44.

879 Raymo, M.E., Ruddiman, W.F., Froelich, P.N. 1988. Influence of late Cenozoic mountain buil-
880 ding on ocean geochemical cycles. Geology 16, 649–653.

881 Riech, V., von Rad, U. 1979. Silica diagenesis in the Atlantic Ocean: diagenetic potential
882 and transformations. *Deep drilling results in the Atlantic Ocean: Continental margins*
883 *and paleoenvironment*, *3*, 315-340.

884 Robert, C. 1981. Santonian to Eocene palaeogeographic evolution of the Rio Grande Rise (Sou-
885 th Atlantic) deduced from clay-mineralogical data (DSDP legs 3 and 39). Palaeogeogra-
886 phy, Palaeoclimatology, Palaeoecology 33, 311–325.

887 Roddaz, M., Viers, J., Brusset, S., Baby, P., Boucayrand, C., Hérail, G. 2006. Controls on
888 weathering and provenance in the Amazonian foreland basin: Insights from major and
889 trace element geochemistry of Neogene Amazonian sediments. Chem Geol, 226, 31–65

890 Roddaz, M., Dera, G., Mourlot, Y., Calvès, G., Kim, J.H., Chaboureau, A.-C., Mounic, S.,
891 Raisson, F. 2021. Provenance constraints on the Cretaceous-Paleocene erosional history of
892 the Guiana Shield as determined from the geochemistry of clay-size fraction of sediments
893 from the Arapaima-1 well (Guyana-Suriname basin). Marine Geology 434, 106233.

894 Ruffell, A., McKinley, J.M., Worden, R.H. 2002.Comparison of clay mineral stratigraphy to
895 other proxy palaeoclimate indicators in the Mesozoic of NW Europe. Philosophical Tran-
896 sactions of the Royal Society London A 360, 675-693.

897 Sapin, F., Davaux, M., Dall'asta, M., Lahmi, M., Baudot, G., and Ringenbach, J.-C. 2016. Post-
898 rift subsidence of the French Guiana hyper-oblique margin : from rift-inherited subsidence
899 to Amazon deposition effect. Geological Society, London, Special Publications, 431 (1),
900 125–144.

901 Söderlund, U., Patchett, P.J., Vervoort, J.D., Isachsen, C.E. 2004. The 176Lu decay constant
902 determined by Lu–Hf and U–Pb isotope systematics of Precambrian mafic intrusions.
903 Earth and Planetary Science Letters 219, 311–324.

904 Stokke, E.W., Jones, M.T., Riber, L., Hflidason, H., Midtkandal, I., Schultz, B.P., Svensen,
905 H.H. 2021. Rapid and sustained environmental responses to global warming: the
906 Paleocene–Eocene Thermal Maximum in the eastern North Sea. Clim. Past 17, 1989–2013.

907 Taylor, S.R., McLennan, S.M. 1985. The Continental Crust: Its Composition and Evolution. An
908 Examination of the Geochemical Record Preserved in Sedimentary Rocks. Blackwell
909 Scientific Publications, Oxford, p. 312.

910 Théveniaut, H., Freyssinet, P. 2002. Timing of lateritization on the Guiana Shield: synthesis of
911 paleomagnetic results from French Guiana and Suriname. Palaeogeography, Palaeocli-
912 matology, Palaeoecology 178, 91-117.

913 Thiry, M. 2000. Palaeoclimatic interpretation of clay minerals in marine deposits: an outlook
914 from the continental origin. Earth-Science Reviews 49, 201-221.

915 Vervoort, J.D., Patchett, P.J., Blichert-Toft, J., Albarède, F. 1999. Relationships between Lu–
916 Hf and Sm–Nd isotopic systems in the global sedimentary system. Earth and Planetary
917 Science Letters 168, 79–99.

918 Vervoort, J.D., Plank, T., Prytulak, J. 2011. The Hf–Nd isotopic composition of marine sedi-
919 ments. Geochim. Cosmochim. Acta 75, 5903–5926.

920 Wang, Y., Huang, C., Sun, B., Quan, C., Wu, J., Lin, Z. 2014. Paleo-CO_2 variation trends and
921 the Cretaceous greenhouse climate. Earth-Science Reviews, 129, 136-147.

922 West, A.J., Galy, A., Bickle, M. 2005. Tectonic and climatic controls on silicate weathering.
923 Earth and Planetary Science Letters 235, 211–228.

924 West, A. J. 2012. Thickness of the chemical weathering zone and implications for erosional and
925 climatic drivers of weathering and for carbon-cycle feedbacks. Geology, 40 (9), 811-814.

926 Weis, D., Kieffer, B., Maerschalk, C., Pretorius, W., Barling, J. 2005. High-precision Pb-Sr-
927 Nd-Hf isotopic characterization of USGS BHVO-1 and BHVO-2 reference materials.
928 Geochemistry, Geophysics, Geosystems 6.

929 Weis, D., Kieffer, B., Maerschalk, C., Barling, J., Jong, J. de, Williams, G.A., Hanano, D.,
930 Pretorius, W., Mattielli, N., Scoates, J.S., Goolaerts, A., Friedman, R.M., Mahoney, J.B.
931 2006. High-precision isotopic characterization of USGS reference materials by TIMS and
932 MC-ICP-MS. Geochemistry, Geophysics, Geosystems 7.

933 White, A.F., Blum, A.E. 1995. Effects of climate on chemical weathering in watersheds.
934 Geochimica et Cosmochimica Acta 59 (9), 1729-1747.

935 Yang, W., Escalona, A. 2011. "Tectonostratigraphic Evolution of the Guyana Basin." AAPG
936 Bulletin 95 (8): 1339-68.

937 Young, GM M., Nesbitt, H., W. 1999. Paleoclimatology and provenance of the glaciogenic
938 Gowganda Formation (Paleoproterozoic), Ontario, Canada: A chemostratigraphic
939 approach. GSA Bulletin 111 (2), 264-274.

940 Zhao, W., Sun, Y., Balsam, W., Lu, H., Liu, L., Chen, J., & Ji, J. (2014). Hf-Nd isotopic
941 variability in mineral dust from Chinese and Mongolian deserts: implications for sources
942 and dispersal. *Scientific Reports*, *4*(1), 1-6.

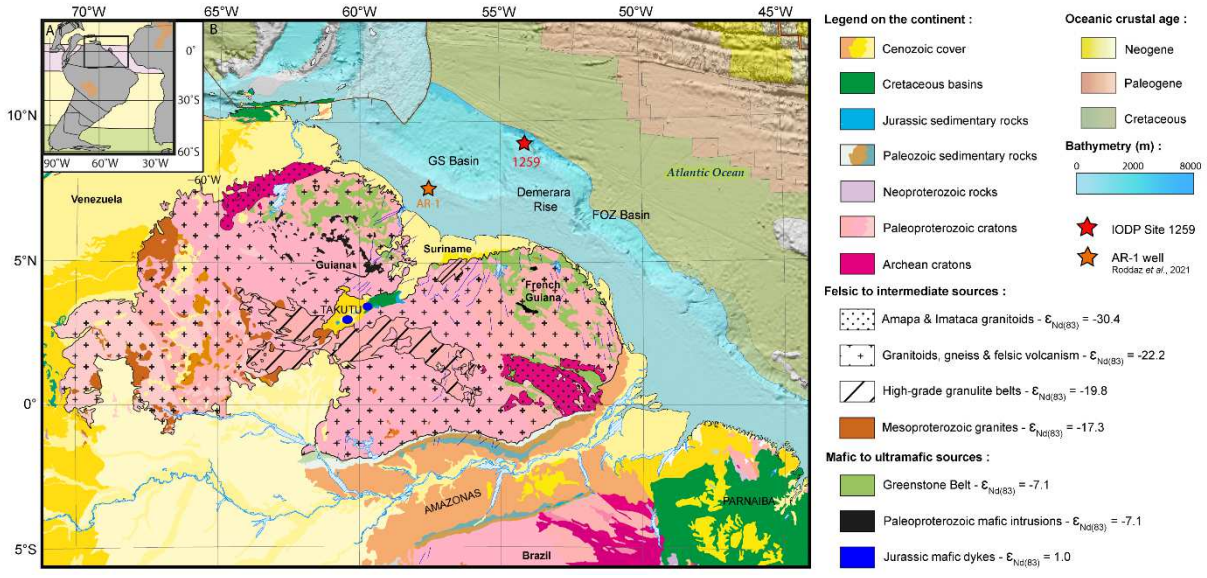

943

944 Figure 1 – A. Palaeogeographic map of the South American continent for the Campanian (83
945 Ma ; www.odsn.de) with the humid climatic belt in pink, the arid climatic belt in yellow, the
946 mid-latitude warm humid belt in green and the evaporitic belts in orange (according to Hay &
947 Floegel, 2012). B. Geological map of the northeastern Brazilian margin with the main $\varepsilon_{Nd(t)}$

948 units of the Guiana Shield from Roddaz *et al*. (2021) calculated at 83 Ma and location of Site

949 1259 and AR-1well from Roddaz et al., 2021.

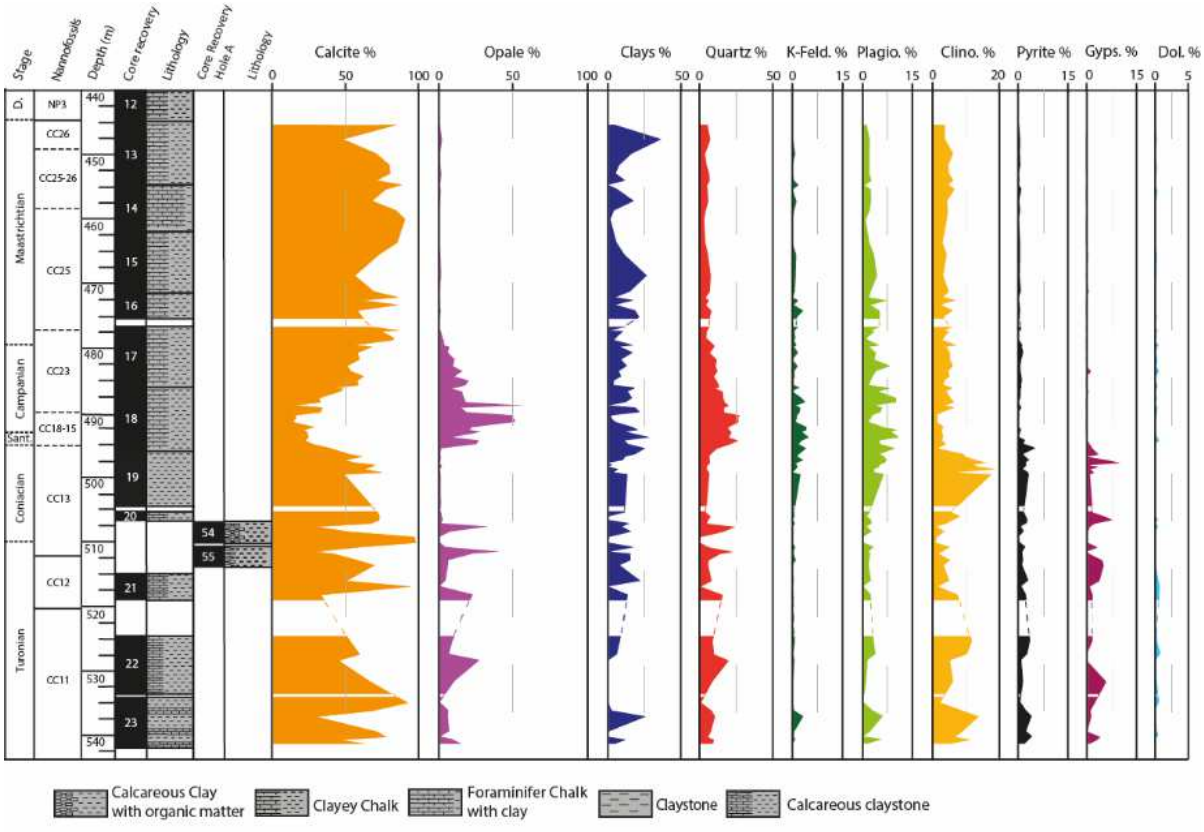

950

951 Figure 2 – Lithology, biostratigraphy and mineralogy at Site 1259. Abbreviations : Sant. =

952 Santonian, D. = Danian.

953

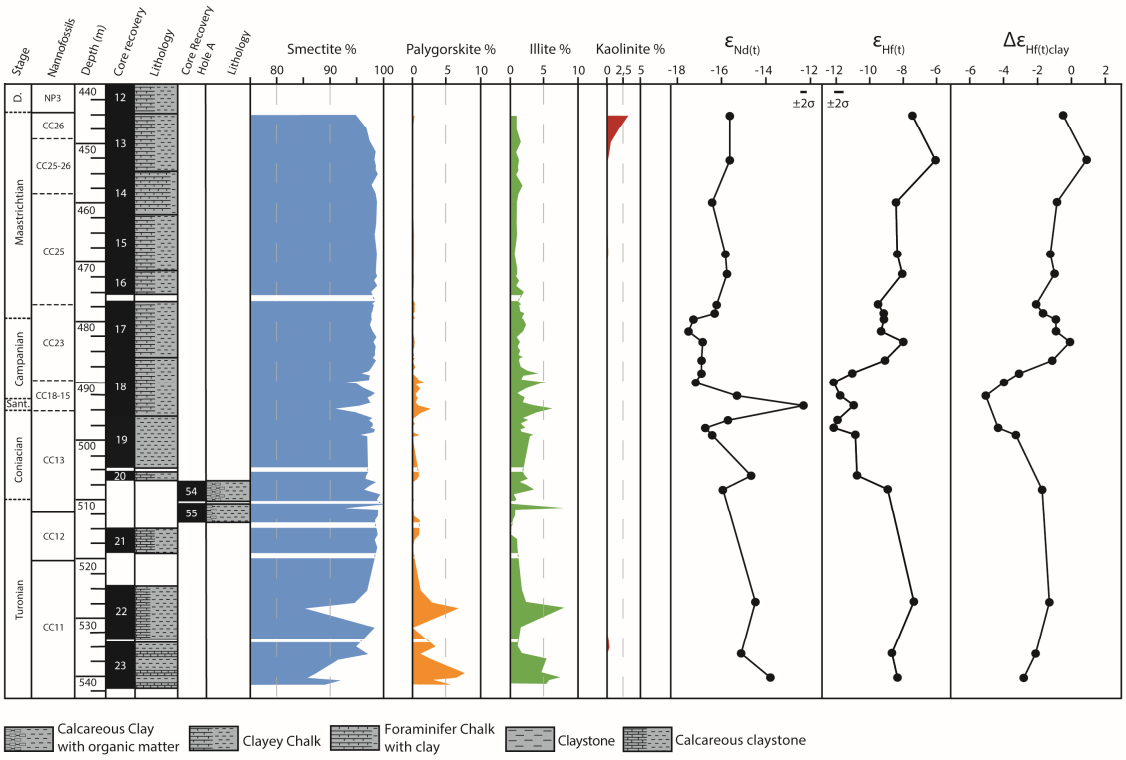

954

955 Figure 3 – Lithology, biostratigraphy, clay mineralogy, $\varepsilon_{Nd(t)}$, $\varepsilon_{Hf(t)}$ and $\Delta\varepsilon_{Hf(t)clay}$ of ODP Site

956 1259. Abbreviations : Sant. = Santonian, D. =Danian. The black bars corresponds to the

957 external reproductibility (2 s.d) of ε_{Nd} and ε_{Hf} based on repeated analyses of JMC 475 and

958 JNDi standards.

959

960

961

962

963

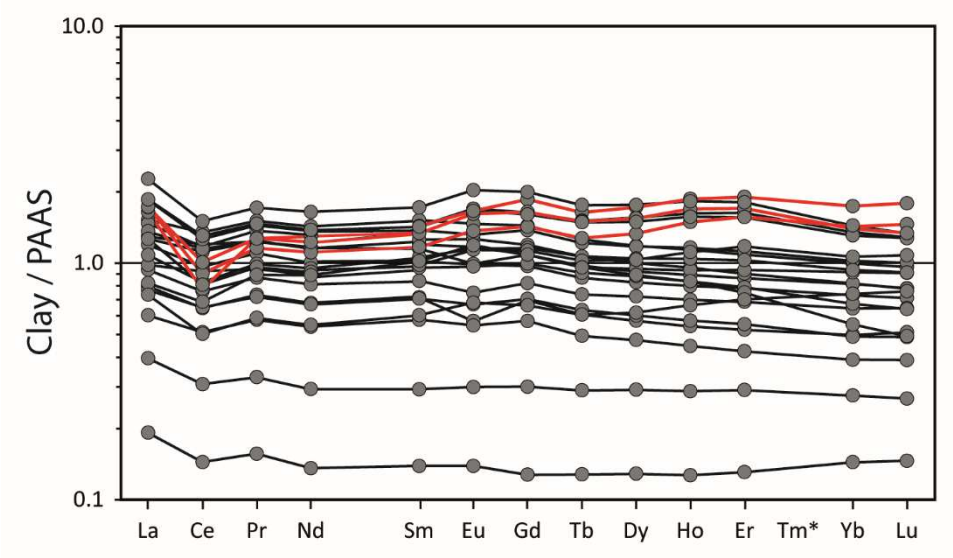

964

965 Figure 4 – Shale-normalized (PAAS ; Taylor and McLennan, 1985) REE patterns for the clay
966 fraction of Site 1259. The three samples in red presents a slight negative Ce anomaly and a
967 slight enrichment in HREE.

968

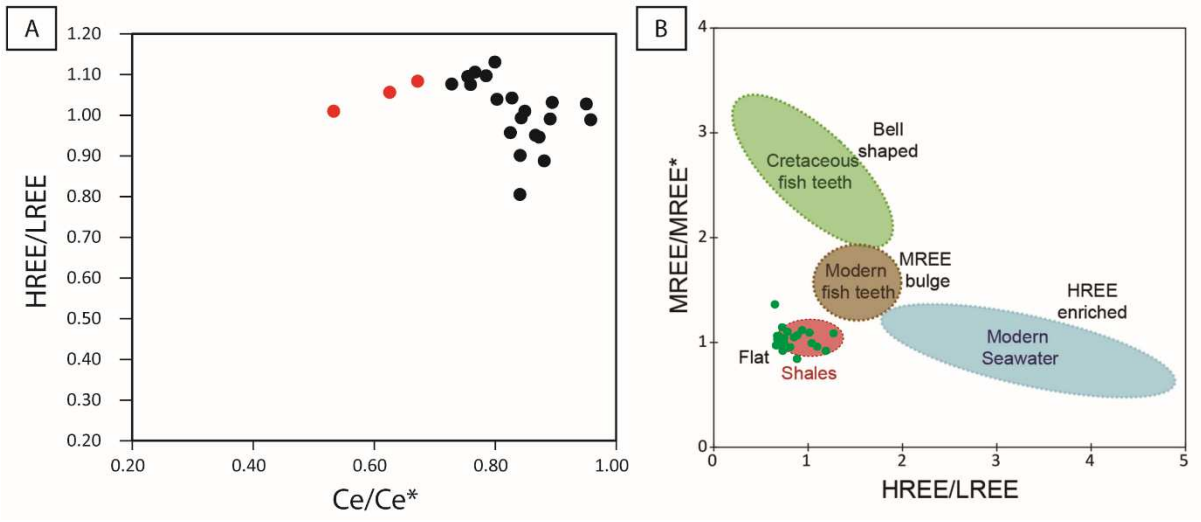

969

970 Figure 5 – A. HREE/LREE vs Ce/Ce* diagram with the three samples in red presenting the
971 most negative cerium anomaly. B. MREE/MREE* vs HREE/LREE diagram. The data of this
972 study appears in green dots and were potted on the diagram of Roddaz et al., 2021. The
973 samples plotted in the "flat" REE patterns end member characteristic of continental clays.

974

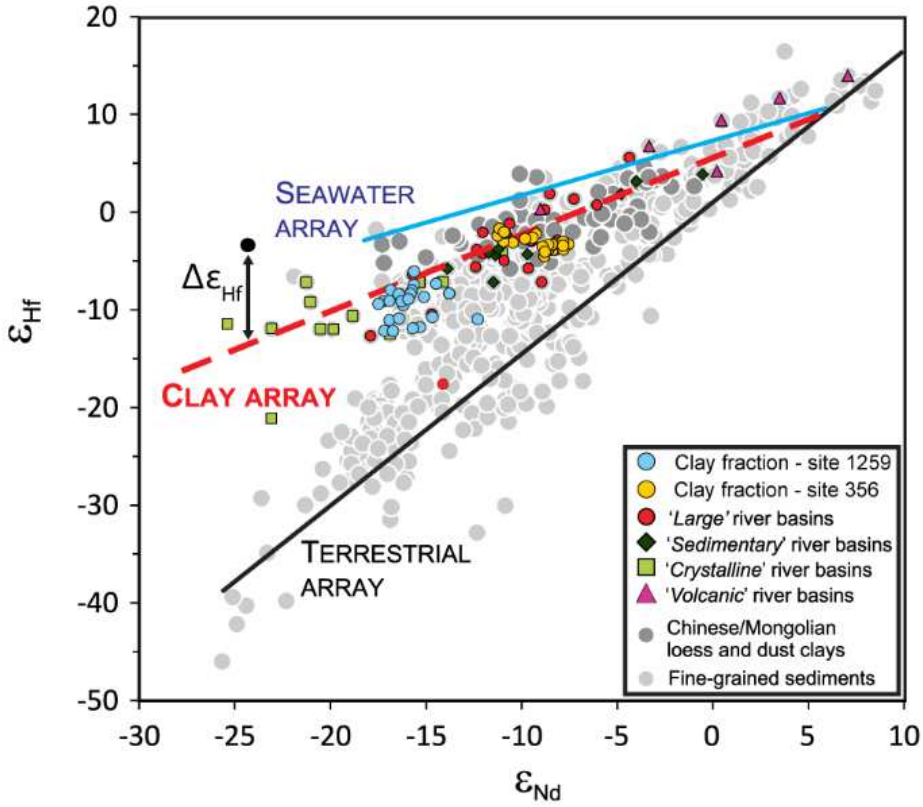

Figure 6 – Nd and Hf isotopic composition of clay-size fractions at Site 1259 and Site 356 (Corentin et al., 2022) together with data for modern river clays (modified from Bayon *et al*, 2016). The Clay Array corresponds to the correlation displayed by ε_{Nd} and ε_{Hf} in modern clay-size fractions (Bayon *et al.*, 2016). $\Delta\varepsilon_{Hf}$ corresponds to the vertical ε_{Hf} deviation of any sample relative to the clay array, which reflects the intensity of chemical weathering.

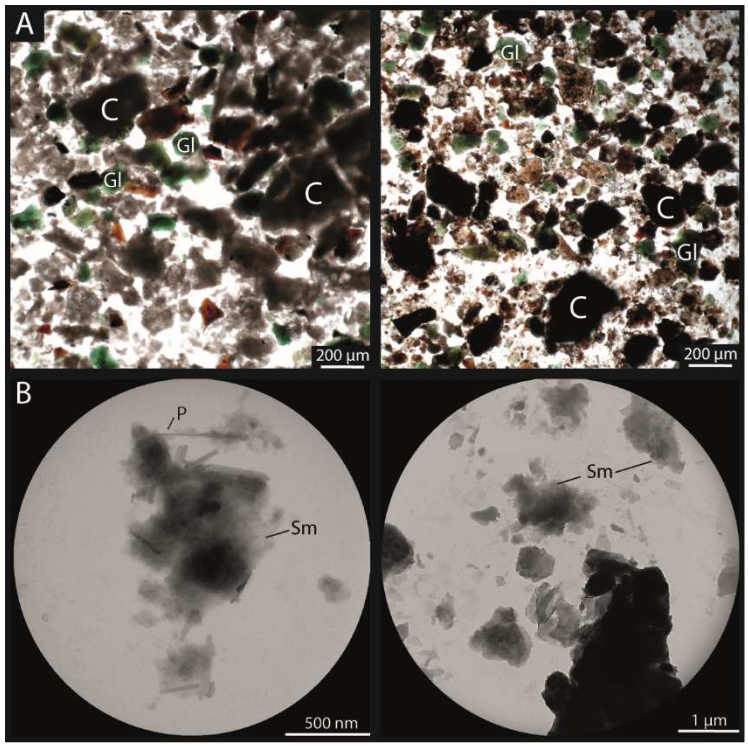

991

992 Figure 7 – A – Smear slides of the samples 18r7w31 (left) and 18rCCw3 (right) containing
993 clay minerals (dark brown) noted "C" and glauconite aggregate (green) noted "Gl". B –
994 Transmission electron micrographs (TEM) of detrital particles of smectite with flake shape
995 (left, sample 22r3w100) and short fibres of detrital palygorskite with smectite particles (right,
996 sample 18r7w80).

997 Figure 8 –Evoluti),

998 (Illite+Chlorite)/Smectite or

999 Site 1259 clay-size fractic *et*

1000 *al.*, 2012) and local $\delta^{18}O_{}$ n.

1001 The grey and black dots or

1002 which both geochemical a ts

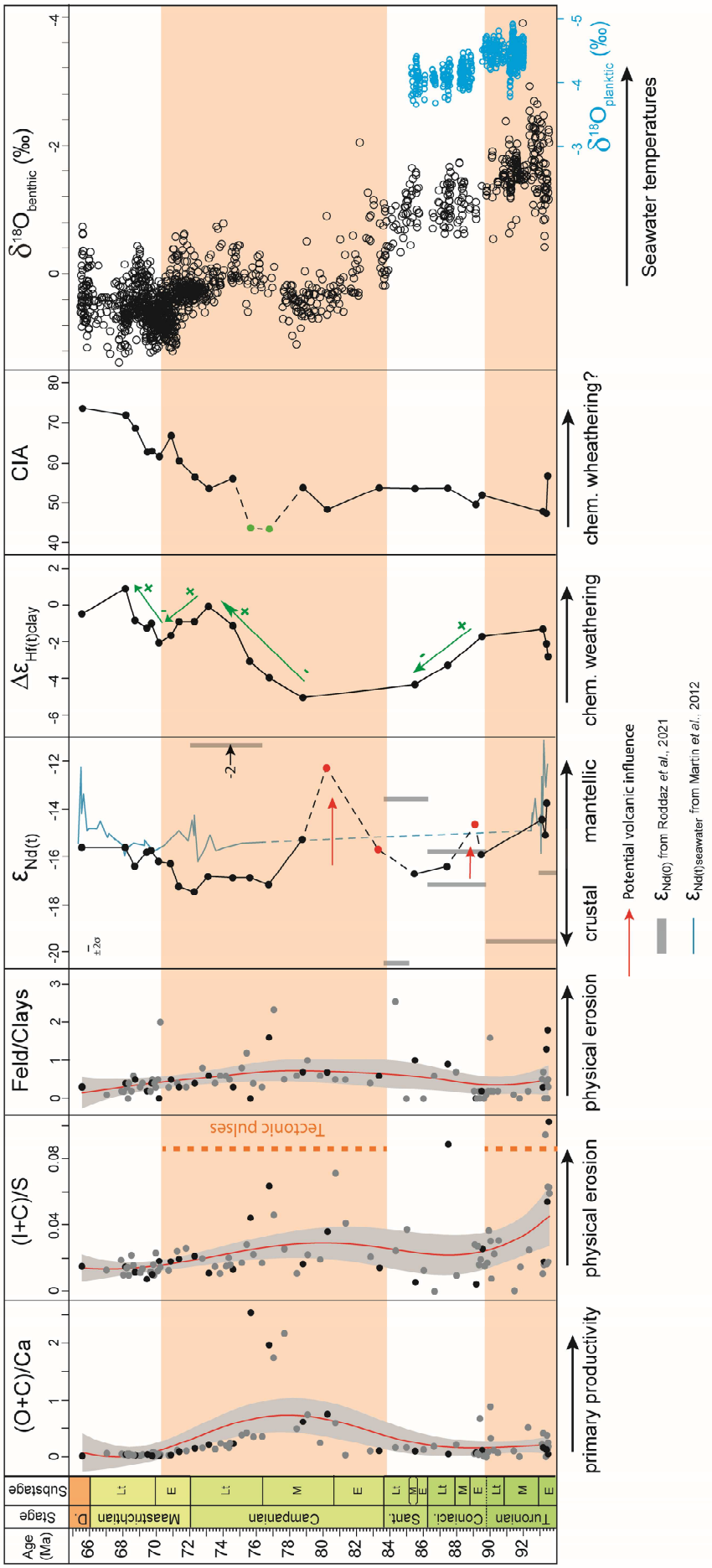

1003 correspond to literature d ts

1004 values (see text for discus 2

1005 s.d) of ε_{Nd} on repeated %

1006 confidence interval have b d

1007 Feld/Clays ratios, with a l d

1008 isotopic compositon of R c

1009 composition of Martin et a n

1010 of chemical weathering on the margin. Abbreviations : Coniac. = Coniacian, Sant. =

1011 Santonian, D. = Danian, E = Early, M = Middle, Lt = Late, chem. = chemical.